arXiv:1006.5126v2 [astro-ph.CO] 9 Sep 2010

THE ATACAMA COSMOLOGY TELESCOPE: PHYSICAL PROPERTIES AND PURITY OF A GALAXY CLUSTER SAMPLE SELECTED VIA THE SUNYAEV-ZEL'DOVICH EFFECT

FELIPE MENANTEAU[1,†,‡], JORGE GONZÁLEZ[2], JEAN-BAPTISTE JUIN[2], TOBIAS A. MARRIAGE[3], ERIK D. REESE[4],
VIVIANA ACQUAVIVA[1,3], PAULA AGUIRRE[2], JOHN WILLIAM APPEL[5], ANDREW J. BAKER[1], L. FELIPE BARRIENTOS[2],
ELIA S. BATTISTELLI[6], J. RICHARD BOND[7], SUDEEP DAS[8], AMRUTA J. DESHPANDE[1], MARK J. DEVLIN[4], SIMON DICKER[4],
JOANNA DUNKLEY[9], ROLANDO DÜNNER[2], THOMAS ESSINGER-HILEMAN[5], JOSEPH W. FOWLER[5], AMIR HAJIAN[7],
MARK HALPERN[10], MATTHEW HASSELFIELD[10], CARLOS HERNÁNDEZ-MONTEAGUDO[11], MATT HILTON[12], ADAM D. HINCKS[5],
RENÉE HLOZEK[9], KEVIN M. HUFFENBERGER[13], JOHN P. HUGHES[1,‡], LEOPOLDO INFANTE[2], KENT D. IRWIN[14], JEFF KLEIN[4],
ARTHUR KOSOWSKY[15], YEN-TING LIN[16], DANICA MARSDEN[4], KAVILAN MOODLEY[12], MICHAEL D. NIEMACK[14],
MICHAEL R. NOLTA[7], LYMAN A. PAGE[5], LUCAS PARKER[5], BRUCE PARTRIDGE[17], NEELIMA SEHGAL[18], JON SIEVERS[7],
DAVID N. SPERGEL[3], SUZANNE T. STAGGS[5], DANIEL SWETZ[4], ERIC SWITZER[19], ROBERT THORNTON[20], HY TRAC[21],
RYAN WARNE[12] AND ED WOLLACK[22],

submitted 2010 June 25; accepted 2010 September 8

ABSTRACT

We present optical and X-ray properties for the first confirmed galaxy cluster sample selected by the Sunyaev-Zel'dovich Effect from 148 GHz maps over 455 square degrees of sky made with the Atacama Cosmology Telescope. These maps, coupled with multi-band imaging on 4-meter-class optical telescopes, have yielded a sample of 23 galaxy clusters with redshifts between 0.118 and 1.066. Of these 23 clusters, 10 are newly discovered. The selection of this sample is approximately mass limited and essentially independent of redshift. We provide optical positions, images, redshifts and X-ray fluxes and luminosities for the full sample, and X-ray temperatures of an important subset. The mass limit of the full sample is around $8.0 \times 10^{14}\, M_{\odot}$, with a number distribution that peaks around a redshift of 0.4. For the 10 highest significance SZE-selected cluster candidates, all of which are optically confirmed, the mass threshold is $1 \times 10^{15}\, M_{\odot}$ and the redshift range is 0.167 to 1.066. Archival observations from *Chandra*, *XMM-Newton*, and *ROSAT* provide X-ray luminosities and temperatures that are broadly consistent with this mass threshold. Our optical follow-up procedure also allowed us to assess the purity of the ACT cluster sample. Eighty (one hundred) percent of the 148 GHz candidates with signal-to-noise ratios greater than 5.1 (5.7) are confirmed as massive clusters. The reported sample represents one of the largest SZE-selected sample of massive clusters over all redshifts within a cosmologically-significant survey volume, which will enable cosmological studies as well as future studies on the evolution, morphology, and stellar populations in the most massive clusters in the Universe.

Subject headings: cosmic background radiation — cosmology: observations — galaxies: distances and redshifts — galaxies: clusters: general — large-scale structure of universe

[1] Rutgers University, Department of Physics & Astronomy, 136 Frelinghuysen Rd, Piscataway, NJ 08854, USA
[2] Departamento de Astronomía y Astrofísica, Facultad de Física, Pontificía Universidad Católica de Chile, Casilla 306, Santiago 22, Chile
[3] Department of Astrophysical Sciences, Peyton Hall, Princeton University, Princeton, NJ 08544, USA
[4] University of Pennsylvania, Physics and Astronomy, 209 South 33rd Street, Philadelphia, PA 19104, USA
[5] Joseph Henry Laboratories of Physics, Jadwin Hall, Princeton University, Princeton, NJ, USA 08544
[6] Department of Physics, University of Rome "La Sapienza", Piazzale Aldo Moro 5, I-00185 Rome, Italy
[7] Canadian Institute for Theoretical Astrophysics, University of Toronto, Toronto, ON, Canada M5S 3H8
[8] Berkeley Center for Cosmological Physics, UC Berkeley, 366 Le Conte Hall, Berkeley, CA 94720
[9] Department of Astrophysics, Oxford University, Oxford, UK OX1 3RH
[10] Department of Physics and Astronomy, University of British Columbia, Vancouver, BC, Canada V6T 1Z4
[11] Max Planck Institut für Astrophysik, Postfach 1317, D-85741 Garching bei München, Germany
[12] University of KwaZulu-Natal, Astrophysics & Cosmology Research Unit, School of Mathematical Sciences, Durban, 4041, South Africa
[13] Department of Physics, University of Miami, 1320 Campo Sano Avenue, Coral Gables, FL 33124

[14] NIST Quantum Devices Group, 325 Broadway Mailcode 817.03, Boulder, CO, USA 80305
[15] University of Pittsburgh, Physics & Astronomy Department, 100 Allen Hall, 3941 O'Hara Street, Pittsburgh, PA 15260, USA
[16] Institute for the Physics and Mathematics of the Universe, The University of Tokyo, Kashiwa, Chiba 277-8568, Japan
[17] Department of Physics and Astronomy, Haverford College, Haverford, PA, USA 19041
[18] Kavli Institute for Particle Astrophysics and Cosmology, Stanford University, Stanford, CA 94305, USA
[19] Kavli Institute for Cosmological Physics, Laboratory for Astrophysics and Space Research, 5620 South Ellis Ave., Chicago, IL, USA 60637
[20] Department of Physics , West Chester University of Pennsylvania, West Chester, PA, USA 19383
[21] Harvard-Smithsonian Center for Astrophysics, Harvard University, Cambridge, MA 02138
[22] Code 553/665, NASA/Goddard Space Flight Center, Greenbelt, MD, USA 20771
† Based on observations made with ESO Telescopes at the La Silla Observatories under programme ID 084.A-0619.
‡ Visiting astronomer, Cerro Tololo Inter-American Observatory, National Optical Astronomy Observatory, which are operated by the Association of Universities for Research in Astronomy, under contract with the National Science Foundation.

1. INTRODUCTION

Clusters of galaxies mark the largest virialized structures in the Universe, and their formation and evolution rates depend on cosmological parameters and the kinematics of the dark matter. The cluster mass function constrains the normalization of the matter power spectrum, typically expressed as σ_8, the root-mean-square (rms) mass fluctuation on a scale of 8 h^{-1}Mpc. As a result, the number of clusters as a function of redshift provides a powerful constraint on both the expansion history of the Universe and the gravitational growth of structure within it (see Carlstrom et al. 2002, and references therein). Both functions are strongly influenced by the matter content Ω_M and the equation of state of the so-called "dark energy" that comprises most of the effective energy density in the Universe. Galaxy clusters also harbor a significant fraction of the visible baryons in the Universe, in the form of a hot intracluster medium that leaves an imprint on the Cosmic Microwave Background (CMB) radiation though the Sunyaev Zel'dovich Effect (SZE) (Sunyaev & Zel'dovich 1972). At frequencies below the SZ null frequency around 218 GHz, clusters appear as small ($\lesssim$ 1mK) decrements in the temperature of the CMB.

Selecting clusters through the strength of their SZE signal has key advantages over other methods of selection: (1) it is relatively independent of redshift, (2) according to simulations, the SZE flux ($Y \equiv \int y\, d\Omega$, where y is the usual Compton y-parameter) should be cleanly related to the cluster mass with low scatter (Motl et al. 2005; Nagai 2006; Reid & Spergel 2006), and (3) according to simulations the SZE signal is more robust to baryonic astrophysics (cooling, AGN feedback). Thus an SZE-selected sample could offer a reliable correlation with cluster mass, which is the key cosmological property, particularly at high redshift. However, optical and X-ray observations are crucial to confirm the SZE detections and calibrate the Y-mass relation predicted by simulations.

The SZE has been the focus of a considerable number of observational efforts over the past three decades. Some of the earliest convincing measurements were made by Birkinshaw et al. (1984) observing at 20 GHz on the 40-m telescope of the Owens Valley Radio Observatory. Each individual cluster detection required many hours of telescope time, typically spread out over several years. By the late 1990's there were still only a dozen or so clusters for which reliable detections had been published (see the review by Birkinshaw 1999).

Large-area cosmological SZE surveys have only now become a reality, thanks to the development of mm-band cameras composed of arrays of order a thousand bolometers located at the focus of large-diameter telescopes (6 to 10 m) offering diffraction-limited imaging at arcminute resolution (a factor of five finer than the *Planck* satellite). Two such experiments, the Atacama Cosmology Telescope (ACT, Fowler et al. 2007) and the South Pole Telescope (SPT, Carlstrom et al. 2009) have surveyed hundreds of square degrees of the southern sky at arcminute resolutions and are reporting the first cluster detections (Staniszewski et al. 2009; Hincks et al. 2009; Vanderlinde et al. 2010). ACT is conducting a wide-area mm-band survey at arcminute resolution with $\simeq$30
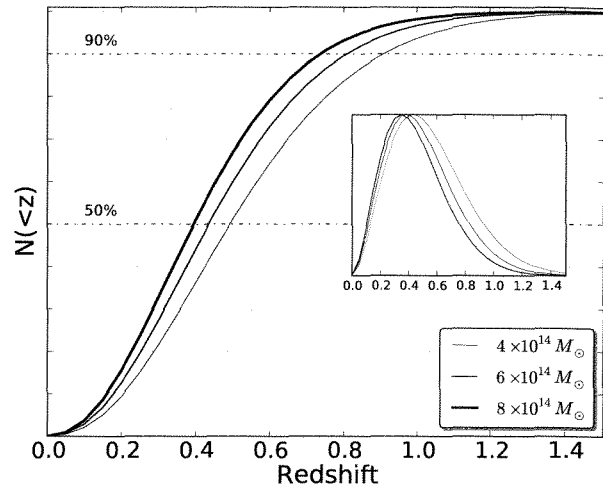

Figure 1. The predicted number of clusters more massive than 4, 6 and 8 $\times 10^{14} M_\odot$ (solid lines) as a function of redshift and normalized to unity from the mass function of Tinker et al. (2008). For reference we show the 50% and 90% fractional completeness levels as dashed lines. The inset shows the normalized differential dN/dz distribution over the same redshift range and mass limits.

μK s$^{1/2}$ array sensitivity to efficiently search for massive galaxy clusters using the SZE. The first ACT SZE clusters detected in the 2008 observation season are reported in Hincks et al. (2009) and the first analysis of the ACT 148 GHz CMB power spectrum reaching to arcminute scales is presented in Fowler et al. (2010).

This paper introduces the first sample of optically-confirmed SZE clusters from the ACT 2008 148 GHz data (see High et al. 2010, for the recent SPT cluster follow-up study) and, for the first time, characterizes observationally the purity of an SZE survey. For this purpose we selected candidate galaxy clusters from ACT maps covering 455 square degrees (a comoving volume of 2.46 Gpc^3 at $z < 1.2$) using a rigorous and uniformly controlled procedure (see Marriage et al. 2010). Subsequently, during the 2009B semester, we imaged candidates in the bands g, r, and i on 4-m class telescopes to confirm the presence of a brightest cluster galaxy (BCG) and an accompanying red sequence of cluster members.

In two companion papers we describe in detail the SZE cluster selection from the ACT data (Marriage et al. 2010) and cosmological constraints from the sample presented here (Sehgal et al. 2010). Throughout this paper we assume a flat cosmology with $H_0 = 100h$ km s^{-1} Mpc^{-1}, $h = 0.7$, and matter density $\Omega_M = 0.3$. The reported magnitudes are always in the AB system. Cluster masses are quoted as M_{200}, which corresponds to integrating the cluster mass within a spherical volume such that the density is 200 times the average density of the Universe at the cluster's redshift.

2. OBSERVATIONAL SETUP

Both ACT and SPT aim to provide a unique sample of massive clusters of galaxies, in principle selected by mass, nearly independently of redshift and over a large area of the sky covering a cosmologically significant volume. Utilizing these cluster samples to constrain cosmology and cluster physics requires empirical characterization of

the SZE selection function.

As the first step in this process we measure the "purity" of the ACT sample, i.e., the fraction of real clusters as a function of the SZE detection significance, using a signal-to-noise limited sample of cluster candidates extracted from the 148 GHz maps. We search for an optical cluster associated with each candidate's SZE decrement. This is relatively straightforward, since for a wide range of mass limits in a ΛCDM cosmology 90% of clusters will lie below $z \approx 0.8$ and are therefore accessible in modest exposures on 4-m class telescopes. To illustrate this point, in Figure 1 we show the expected number of clusters of galaxies more massive than 4, 6 and $8 \times 10^{14} M_{\odot}$ as a function of redshift from the mass function of Tinker et al. (2008). This range in mass limit covers the current relevant range for ACT. A key requirement of our observing plan is efficient multi-band optical imaging of ACT cluster candidates. Unfortunately, the current generation of large and wide format CCD mosaic cameras are not ideally suited for this task as their long read-out times (typically between $100 - 200$ s) often become comparable to the required exposure times to find L^* (the characteristic Schechter luminosity) ellipticals at $z \simeq 1$, resulting in significant time overheads. For our observations, we decided instead to trade the large field-of-view for smaller but faster readout CCD cameras (around 10 s) that allow us to move rapidly from target to target and secure multi-band imaging for the central $5'$ of the clusters, sufficient for the identification process because of the accurate astrometry of the mm-band data (see below).

The number of nights required for this measurement is set by several factors, but the basic requirement is unambiguously detecting all optical clusters out to a redshift of $z \approx 0.8$ (as shown in Figure 1), where we can detect a high fraction ($\simeq 90\%$) of *all* massive clusters even for a conservative mass threshold of $4 \times 10^{14} M_{\odot}$. The optical cluster detection requires seeing a cluster red sequence (i.e., early-type galaxies with luminosities less than L^*). Our exposure times are therefore determined by the observed $i-$band magnitudes of low-luminosity ($\simeq 0.4L^*$) red-sequence galaxies at $z \simeq 0.8$, so that we can confidently identify clusters using the overdensity of red galaxies. In addition to being dominated by a red sequence of galaxies, massive clusters exhibit another distinctive signature, the presence of a BCG (typically with luminosity of a few L^*). Our observation plan is hence designed to detect both of these features of real clusters (BCG and red-sequence) for 90% of the SZE candidates (i.e., $z < 0.8$). For most of the remaining clusters at $z > 0.8$ (estimated to be only 10% of the total number) we will be able to detect the presence of a BCG as well as some of the brightest cluster members.

3. ANALYSIS

3.1. *Selection of ACT SZE Cluster Candidates*

ACT is a dedicated arcminute resolution CMB experiment consisting of a 6-m off-axis Gregorian telescope located at 5190m on Cerro Toco, near the Chajnantor Plateau, in the Atacama Desert in northern Chile (see Fowler et al. 2007; Hincks et al. 2009; Fowler et al. 2010; Swetz et al. 2010, for a complete description). The SZE cluster selection for this work is based on 148 GHz data

from the ACT 2008 southern survey using the Millimeter Bolometer Array Camera (MBAC; Niemack et al. 2008) on the ACT focal plane and with band centers at 148 GHz, 218 GHz and 277 GHz. The 2008 southern survey area is 9° wide, centered on declination $-53.5°$, and extends from right ascension 19^h to 24^h and 00^h to $07^h 30^m$. A total of 850 hours of data with an average of 680 working detectors at 148 GHz (yielding a data volume of 3200 GB) are used to make the microwave sky map. Relative detector pointings are established through observations of Saturn which has a high enough signal-to-noise ratio to allow a pointing fit for each detector. Absolute pointings for the survey are iteratively solved by comparing ACT radio source detections. The resulting rms uncertainty in the reported positions is $5''$ (Fowler et al. 2010).

The data are calibrated with 6% precision to Uranus by extrapolating the lower frequency WMAP7 Uranus calibration (Weiland et al. 2010). A highly-parallelized preconditioned conjugate gradient code is used to simultaneously solve for the maximum likelihood millimeter-wave map and correlated noise (e.g., from large-scale atmospheric emission).

Cluster candidates were detected in a 148 GHz, 455 square-degree submap from the ACT 2008 observing season. The submap lies between right ascensions $00^h 12^m$ and $07^h 08^m$ and declinations $-56° 11'$ and $-49° 00'$. The median noise level in this submap in terms of the decrement amplitude is 31μK. After masking bright sources from the ACT 148 GHz source catalog, the map is match-filtered in the Fourier domain using the isothermal β-model ($\beta = 2/3$) convolved with the ACT 148 GHz beam and models for the ACT noise, primary CMB fluctuations, and undetected sources. The form of the filter (Melin et al. 2006; Haehnelt & Tegmark 1996) is

$$\Phi(\vec{k}) = \frac{\tilde{B}_{\theta_c}^{*}(\vec{k}) \mid \tilde{T}_{other}(\vec{k}) \mid^{-2}}{\int \tilde{B}_{\theta_c}^{*}(\vec{k'}) \mid \tilde{T}_{other}(\vec{k'}) \mid^{-2} \tilde{B}_{\theta_c}(\vec{k'}) d\vec{k'}} \quad (1)$$

where $\tilde{B}_{\theta_c}(\vec{k'})$ is the Fourier transform of the beam-convolved β-model with critical radius θ_c, and $\tilde{T}_{other}(\vec{k'})$ is the transform of the noise obtained from a combination of ACT difference maps, the WMAP5 primary CMB signal, and the undetected sources (and clusters) based on the amplitudes of Fowler et al. (2010). The map is filtered using β-models with critical radii from $0.25'$ to $4.0'$ in $0.25'$ steps. For a given filter, the SNR of a cluster detection is defined as the ratio of decrement amplitude to total rms. The reported significance of a cluster detection corresponds to the filter which maximizes this SNR. Furthermore, any detection that was not detected at greater than SNR>3.5 in at least four conjoined pixels was discarded.

During 2009B the ACT data reduction pipeline and cluster extraction algorithms evolved such that everything from pointing to data selection to the matched filter for the final candidate list changed from one observing run to the next. Thus we observed more SZE candidates than used in the purity study (although we report all confirmed cluster detections regardless of its origin). Despite this inefficiency the optical study completely vetted a SNR-ordered list of candidates selected in the manner described above. A final caveat is that af-

Table 1
2009B Approved Observing Runs

Run	Tel.	Camera	Dates	Nights	TAC
1	SOAR	SOI	2009, Aug 22-23	0/2	CNTAC
2	NTT	EFOSC	2009, Oct 22-26	3/4	ESO/Chile
3	SOAR	SOI	2009, Dec 9-12	4/4	NOAO

Note. — For run 1 we applied for SOAR time but were reassigned by the CNTAC to the CTIO/Blanco 4-m telescope due to re-aluminization of the SOAR mirror.

ter the optical observing season ended, the ACT pipeline continued to evolve such that the finalized candidate list tested here is not identical to the list presented in Marriage et al. (2010). While the SNR of the high significance candidates remains similar between this study and Marriage et al. (2010), the fainter candidates differ in SNR with some of the faintest candidates falling below the SNR threshold of the Marriage et al. list. This is expected: different map-making configurations weight the data in different ways, and a faint candidate which is decrement-boosted by noise in one realization of map may not be boosted in the next.

3.2. *2009B Optical Observing Campaign*

During the 2009B semester we were awarded a total of 10 dark nights for this project in three observing runs on 4-m class telescopes obtained through different Telescope Allocation Committees (TACs). Unfortunately our first run (2 nights), which occurred during the Chilean winter, was completely lost due to snow and no data were obtained (09B-1007, PI:Infante). The next two observing runs had optimal conditions and enabled the successful completion of our program. In Table 1 we summarize the telescopes, instruments, dates, number of good (photometric) nights, and the TACs that awarded the time.

In the run during October 22-26, 2009 we used the ESO Faint Object Spectrograph and Camera (EFOSC) on the 3.6-m NTT on La Silla (084.A-0619, PI:Barrientos) and observed SZE candidates using the Gunn *gri* filter, with exposure times of 270 s (3 × 90 s), 360 s (3 × 120 s) and 1100 s (4 × 275 s) in *g*, *r* and *i* respectively. EFOSC consists of a 2048 × 2048 pixel thinned, AR coated CCD#40 detector projecting a 4.1′ × 4.1′ field-of-view at 0.2408″/pixel (2 × 2 binning) on the sky. For the three first nights of this run atmospheric conditions were photometric with seeing 0.″7 − 1″. The last and fourth night of the run was lost due to clouds and no data were taken. Throughout the run we also observed photometric standards from the Southern Hemisphere Standards Stars Catalog (Smith et al. 2007) to calibrate our data.

For our final run, we used the SOAR Optical Imager (SOI) on the 4.1-m SOAR Telescope on Cerro Pachón (09B-0355, PI: Menanteau) for four nights from December 9-12, 2009. SOI is a bent-Cassegrain mounted optical imager using a mini-mosaic of two E2V 2048 × 4096 pixel CCDs to cover a 5.26′ × 5.26′ field-of-view at a scale of 0.″154/pixel (2 × 2 binning). For our cluster search we used the same exposure times as in the NTT using the SDSS *gri* filter set. For three cluster candidates presumed to be at high redshift we obtained observations twice as long as the nominal exposure times and additional deep 2200s (8 × 275s) *z*-band observations. The
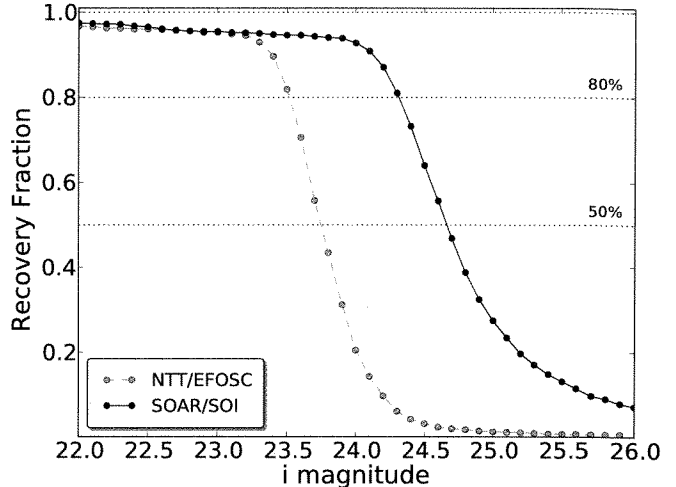

Figure 2. The recovery fraction of simulated elliptical galaxies, using a de Vaucouleurs profile, as a function of the observed *i*-band magnitude for the NTT (dashed line) and SOAR (solid line) observations. We show for reference the 50% and 80% recovery fraction levels.

run conditions were optimal and all four nights were photometric, with seeing in the range 0.″5 − 1″. We observed photometric standard stars using the same set and method as we did for the earlier NTT run.

3.3. *Optical Data Reduction*

For the optical analysis we take advantage of an existing imaging data pipeline that takes us from raw data to galaxy catalogs. We use a modified version of the Python-based Rutgers Southern Cosmology image pipeline (Menanteau et al. 2009, 2010) to process the data from the NTT and SOAR runs. The initial standard CCD processing steps are performed using IRAF[25]/ccdproc tasks via the STScI/PyRAF[26] interface. The fast read-out time of the CCDs allowed us to accommodate multiple dithered exposures for each targeted cluster candidate. In our cluster observations we followed a 10″ off-center 3–, 3–, and 4–point dither pattern in the *g*, *r*, and *i* bands, respectively, which helped to avoid saturated stars, remove chip defects and artifacts, and cover the 10″ gap between CCDs in the SOI camera. Individual science frames were astrometrically recalibrated before stacking by matching sources with stars from the US Naval Observatory Catalog. Observed fields with photometric standard stars from the Smith et al. (2007) catalog were processed in the same fashion and we obtained a photometric zero-point solution in AB magnitudes for each observing night. For each targeted cluster we associated all science frames in all filters and aligned and median combined them into a common pixel reference frame using SWarp (Bertin 2006) to a plate scale of 0.″2408/pixel for the NTT and 0.″1533/pixel for SOAR. Source detection and photometry for the science catalogs were performed using SExtractor (Bertin &

[25] IRAF is distributed by the National Optical Astronomy Observatory, which is operated by the AURA under cooperative agreement with NSF
[26] PyRAF is a product of the Space Telescope Science Institute, which is operated by AURA for NASA
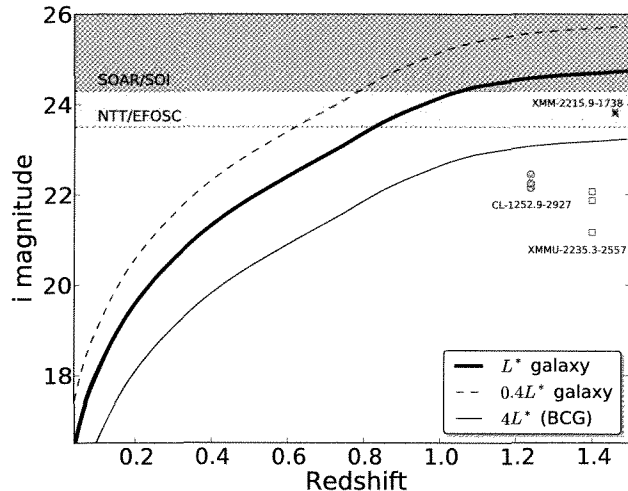
Figure 3. The observed i-band magnitudes of L^*, $0.4L^*$ and $4L^*$ (BCG) early-type galaxies as a function of redshift. We use L^* as defined Blanton et al. (2003) for the population of red galaxies at $z = 0.1$ and allow it to passively evolve with redshift. We show in different gray levels the 80% completeness limits for the NTT and SOAR observations. In other words, at magnitudes below the gray band we detect elliptical galaxies with at least 80% completeness. We also show the observed magnitudes for the three brightest galaxies in three high redshift clusters.

Arnouts 1996) in dual-image mode in which sources were identified on the i−band images using a 1.5σ detection threshold, while magnitudes were extracted at matching locations from all other bands. The computed magnitudes in our catalogs were corrected for Galactic dust absorption in each observed band utilizing the infrared maps and C routines provided by Schlegel et al. (1998). This step is particularly important for obtaining unbiased colors, required for accurate photometric redshifts, as significant variations occur over the large area covered by the ACT 2008 survey region.

The final step in our pipeline involves computing the photometric redshift and redshift probability distributions, $p_{BPZ}(z)$, for each object using the spectral energy distribution (SED) based BPZ code (Benítez 2000) with a flat prior. We compute photometric redshifts using the dust-corrected g, r, i isophotal magnitudes, as defined by the i-band detection and the BPZ set of template spectra described in Benítez et al. (2004) which is based on the templates from Coleman et al. (1980) and Kinney et al. (1996). This set consists of El, Sbc, Scd, Im, SB3, and SB2 and represent the typical SEDs of elliptical, early/intermediate type spiral, late-type spiral, irregular, and two types of starburst galaxies respectively.

3.4. Galaxy Completeness and Recovery Fraction

The exposure times for our observations were designed to confidently detect sub-L^* early-type galaxies up to $z \approx 0.8$ and BCGs at $z > 1.0$ in order to confirm the presence of a galaxy cluster. In order to assess the depth reached by the observations as well as the differences between telescopes, we performed Monte Carlo simulations to estimate the recovery fraction of early-type galaxies as a function of magnitude in each of our observing runs. We used the IRAF/artdata package to create simulated data sets for the NTT and SOAR observations, which

were subsequently processed through our pipeline using the same detection and extraction procedures as for the science images. Within artdata we used the mkobjects task to draw artificial elliptical galaxies on science fields as de Vaucouleurs profiles with the same noise properties as the real data. We scaled the surface brightness of the galaxy profiles according to their magnitude for a range of assumed sizes ($1 - 7$ kpc, but converging to the typical image seeing at the faint limits). Using this procedure we generated 20 and 25 artificial elliptical galaxies for the NTT and SOAR datasets respectively over a wide range of magnitudes ($19 < i < 27$) sampled at small ($\Delta_{mag} = 0.1$) steps. We repeated this 10 times for each dataset at each step. At each magnitude step we matched the recovered galaxies in the simulations with the input positions from the artificial catalogs. In Figure 2 we show the recovered fraction of galaxies as a function of the input i-band magnitude for the NTT and SOAR dataset, as well as the 80% and 50% levels for reference. From this exercise we conclude that we reach 80% completeness at $i = 23.5$ and $i = 24.3$ for elliptical galaxies for the NTT and SOAR datasets respectively. We emphasize that we followed the same observing strategy (i.e. same filter set, dithering pattern and exposure times) for both runs and therefore the relatively large difference (0.8 mag) in the completeness limit is likely due to a combination of telescope size (3.6-m vs 4.1-m), CCD sensitivity and telescope throughput. The re-aluminization of the SOAR primary mirror in November 2009, just before our run, might have played a role in the higher sensitivity of the SOAR imaging.

We can use the completeness limits estimated from our simulations to determine how far in redshift we can "see" massive clusters. For this, we compare the completeness limits of our observations to the expected and observed (i.e. known) apparent magnitudes of galaxies *in* clusters as a function of redshift. We estimated the expected apparent galaxy i-band magnitude as a function of redshift using L^* as defined for the population of red galaxies by Blanton et al. (2003) at $z = 0.1$ and allowing passive evolution according to a solar metallicity Bruzual & Charlot (2003) $\tau = 1.0$ Gyr burst model formed at $z_f = 5$. We show this in Figure 3 for a range of luminosities ($0.4L^*$, L^* and $4L^*$) aimed at representing the cluster members from the faint ones to the BCG. We also show as different gray levels the 80% completeness as determined by the simulations for the NTT and SOAR run, which provides evidence that we can reach typical L^* galaxies to $z \approx 0.8$ for both datasets (and $z \approx 1$ for the SOAR data). We also compare the depth of our imaging campaign to the observed i-band apparent magnitudes of galaxies in three massive high redshift ($z > 1.2$) clusters for which we could find suitable data in the literature for comparison. In Figure 3 we plot the observed magnitude of the three brightest galaxies for the clusters RDCS 1252.9−2927 (Blakeslee et al. 2003; Rosati et al. 2004) at $z = 1.237$, XMMU J2235.3−2557 (Mullis et al. 2005; Rosati et al. 2009) at $z = 1.393$ and XMMXCS J2215.9−1738 (Stanford et al. 2006; Hilton et al. 2009) at $z = 1.457$. We conclude that, with the possible exception of a cluster like XMMXCS J2215.9−1738 observed during the NTT run, we comfortably detect luminous galaxies in clusters at high redshift. This provides further evidence that our observation's integration times allow us to confidently

Table 2
ACT 2008 clusters

ACT Descriptor	R.A. (J2000)	Dec. (J2000)	Redshift	SNR	Alt Name
ACT-CL J0145-5301	01:45:03.6	-53:01:23.4	0.118 [a]	4.7 (4.0)	Abell 2941
ACT-CL J0641-4949	06:41:37.8	-49:46:55.0	0.146 [b]	4.9 (4.9)	Abell 3402
ACT-CL J0645-5413	06:45:29.5	-54:13:37.0	0.167 [a]	7.1 (7.1)	Abell 3404
ACT-CL J0638-5358	06:38:49.4	-53:58:40.8	0.222 [a]	10.6 (10.0)	Abell S0592
ACT-CL J0516-5430	05:16:37.4	-54:30:01.5	0.294 [c]	5.2 (4.7)	Abell S0520/SPT-CL J0516-5430
ACT-CL J0658-5557	06:58:33.1	-55:57:07.2	0.296 [d]	11.6 (11.5)	1E0657-56 (Bullet)
ACT-CL J0245-5302	02:45:35.8	-53:02:16.8	0.300 [e]	8.3 (9.1)	Abell S0295
ACT-CL J0217-5245	02:17:12.6	-52:44:49.0	0.343 [f]	4.5 (4.1)	RXC J0217.2-5244
ACT-CL J0237-4939	02:37:01.7	-49:38:10.0	0.40 ± 0.05	4.9 (3.9)	
ACT-CL J0707-5522	07:07:04.7	-55:23:08.5	0.43 ± 0.06	4.2 (...)	
ACT-CL J0235-5121	02:35:45.3	-51:21:05.2	0.43 ± 0.07	5.7 (6.2)	
ACT-CL J0330-5227	03:30:56.8	-52:28:13.7	0.440 [g]	7.4 (6.1)	Abell 3128(NE)
ACT-CL J0509-5341	05:09:21.4	-53:42:12.3	0.461 [h]	4.4 (4.8)	SPT-CL J0509-5342
ACT-CL J0304-4921	03:04:16.0	-49:21:26.3	0.47 ± 0.05	5.0 (3.9)	
ACT-CL J0215-5212	02:15:12.3	-52:12:25.3	0.51 ± 0.05	4.8 (4.9)	
ACT-CL J0438-5419	04:38:17.7	-54:19:20.7	0.54 ± 0.05	8.8 (8.0)	
ACT-CL J0346-5438	03:46:55.5	-54:38:54.8	0.55 ± 0.05	4.4 (4.4)	
ACT-CL J0232-5257	02:32:46.2	-52:57:50.0	0.59 ± 0.07	5.2 (4.7)	
ACT-CL J0559-5249	05:59:43.2	-52:49:27.1	0.611 [i]	5.1 (5.1)	SPT-CL J0559-5249
ACT-CL J0616-5227	06:16:34.2	-52:27:13.3	0.71 ± 0.10	6.3 (5.9)	
ACT-CL J0102-4915	01:02:52.5	-49:14:58.0	0.75 ± 0.04	8.8 (9.0)	
ACT-CL J0528-5259	05:28:05.3	-52:59:52.8	0.768 [h]	4.7 (...)	SPT-CL J0528-5300
ACT-CL J0546-5345	05:46:37.7	-53:45:31.1	1.066 [h]	7.2 (6.5)	SPT-CL J0546-5345

Note. — R.A. and Dec. positions denote the BCG position in the optical images of the cluster. The SZE position was used to construct the ACT descriptor identifiers. Clusters with uncertainty estimates on their redshifts are those systems for which only photometric redshifts are available from the NTT and SOAR *gri* imaging. The values of SNR in parentheses are the current values from Marriage et al. (2010), while the others are the ones used in this study

[a] spec-z from de Grandi et al. (1999)
[b] spec-z from Jones et al. (2009)
[c] spec-z from Guzzo et al. (1999)
[d] spec-z from Tucker et al. (1998)
[e] spec-z from Edge et al. (1994)
[f] spec-z from Böhringer et al. (2004)
[g] spec-z from Werner et al. (2007)
[h] spec-z from Infante et al. (2010), Brodwin et al. (2010)
[i] spec-z from High et al. (2010)

identify real SZE clusters up to $z \approx 1.2 - 1.4$, below this redshift according to ΛCDM model $> 99\%$ of all clusters more massive $8 \times 10^{14} M_\odot$ should reside. In Section 4.7 we further discuss the possibility of missing $z > 1.2$ massive clusters in our observations.

3.5. *Additional Imaging Data*

A number of the SZE cluster candidates were associated with previously known clusters at lower redshifts. For a few of these we obtained new NTT/SOAR *gri* observations in order to calibrate our photometric redshift and to test our identification procedure; however, for the most part these were avoided and we relied on public archival imaging and on data from other existing programs to compare with the SZE sources.

AS0295 and AS0592 are included among the low redshift SZE clusters reported by Hincks et al. (2009) and are the focus of a separate observing program by our group (09B-0389, PI:Hughes) aimed at obtaining weak lensing masses using deep V and R observations. These were obtained using the MOSAIC camera on the Blanco 4-m telescope on January 9, 2010 under photometric conditions.

1E0657−56 (the Bullet Cluster) has been extensively observed at different wavelengths. Here we show the optical observations of the cluster central region taken

with the Advanced Camera for Surveys aboard the Hubble Space Telescope (HST) (GO:10200, PI:Jones and GO:10863, PI:Gonzalez) using the F606W (V), F814W (I) and F850LP (z) filters which were taken from the HST archive[27].

For RXCJ0217.2−5244 we used our own pipeline to process raw V (720s) and R (1200s) images obtained from the ESO archive[28] (70.A-0074-A, PI:Edge) utilizing the SUSI camera on the NTT on Oct 7 and 12, 2002.

A fraction of the area covered by ACT overlaps with the 41 deg^2 *griz* imaging from the CTIO 4-m telescope MOSAIC camera on the 05hr field from the Southern Cosmology Survey (Menanteau et al. 2010). We used these data to search for optical identification of SZE cluster candidates in the region to avoid re-targeting with the NTT and SOAR telescopes.

4. RESULTS

4.1. *The ACT SZE Cluster Sample*

Our analysis has resulted in a sample of 23 optically-confirmed SZE clusters selected from 455 square-degrees of ACT data between $0.1 < z < 1.1$. Nine of these clusters, such as 1E0657−56 (the Bullet Cluster), Abell

[27] http://archive.stsci.edu/
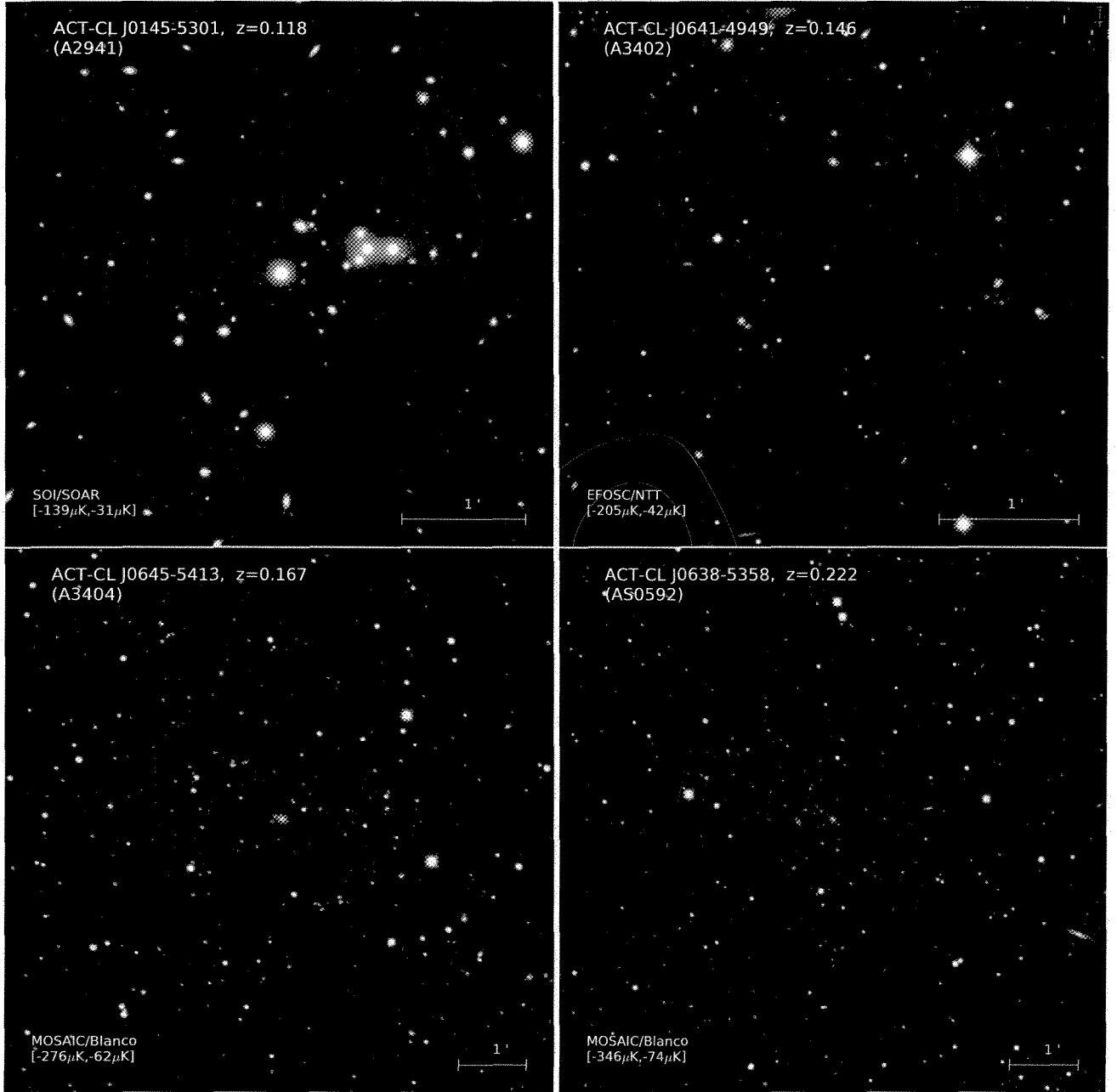[28] http://archive.eso.org/

Figure 4. Composite color images for ACT-CL J0145-5301 (Abell 2941), ACT-CL J0641-4949 (Abell 3402), ACT-CL J0645-5413 (Abell 3404) and ACT-CL J0638-5358 (Abell S00592). The horizontal bar shows the scale of the images, where north is up and east is left. White contours show the 148 GHz SZE maps with the minimum and maximum levels, in μK, displayed between brackets.

S0592, and Abell 3404 are well known and appear at low redshift ($z < 0.4$); and four systems in our sample have been reported as SZE-selected clusters by SPT in their area overlapping with the ACT coverage. Three of these systems (ACT-CL J0509−5341, ACT-CL J0528−5259, and ACT-CL J0546−5345) were originally reported as SZE-selected clusters by Staniszewski et al. (2009), with optical and X-ray properties subsequently studied by us (Menanteau & Hughes 2009), and ACT J0559−5249 has been recently reported by High et al. (2010). About two-thirds of the clusters we present here (14), however, are new SZE-discovered systems (4 of which overlap with

the SPT cluster sample of High et al. 2010) previously unrecognized in the optical or X-ray bands; ten of these are entirely new discoveries by ACT, with photometric redshifts ranging from $z = 0.4$ to $z = 0.8$. All of the new clusters are optically quite rich and a number show strong lensing arcs (see section 4.2). We present the full list of clusters, positions and redshifts (photometric in some cases) in Table 2. In Figures 4-10 we show the composite color optical images of all clusters in our sample with the ACT 148 GHz contours (six equally-spaced between the minimum and maximum levels in μK shown between brackets) overlaid on the images.
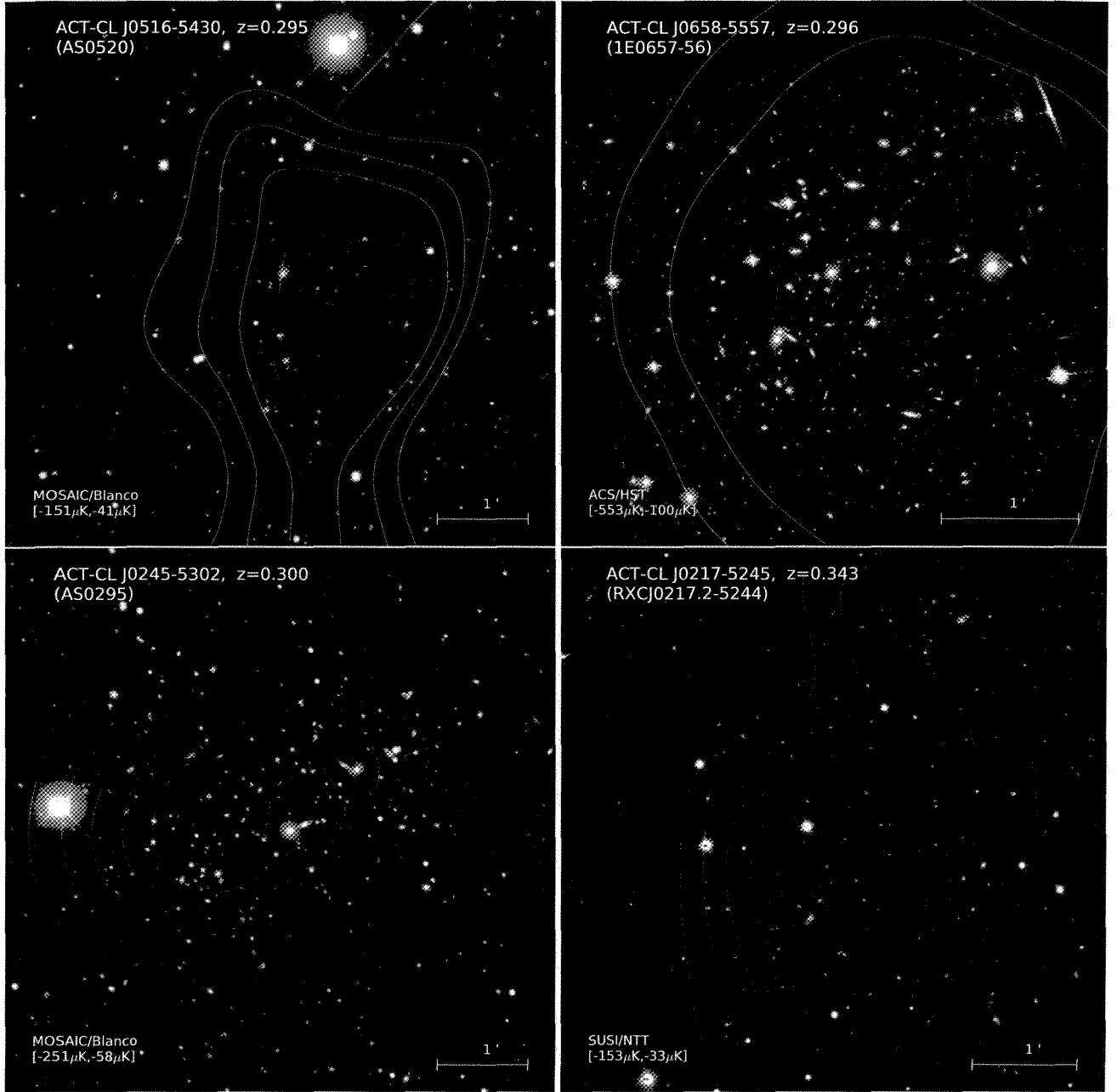
Figure 5. Composite color images for ACT-CL J0516-5430 (Abell S0520), ACT-CL J0658-5557 (Bullet), ACT-CL J0245-5302 (Abell S0295) and ACT-CL J0237-4939 (RXC J0217.2-5244). The horizontal bar shows the scale of the images, where north is up and east is left. White contours show the 148 GHz SZE maps with the minimum and maximum levels, in μK, displayed between brackets.

In the following sections we provide detailed information on individual clusters in the sample in increasing redshift order.

4.1.1. *ACT-CL J0145-5301 (Abell 2941)*

Abell 2941 is the lowest redshift cluster in our sample and it was originally reported by Sérsic (1974) as a compact cluster in his list of peculiar galaxies, groups and clusters based on the Maksutov plate collection of the Universidad de Chile's Observatorio Astronomico. It was later included by Abell et al. (1989) as an optically rich cluster, with R=2 according to the Abell (1958) classifi-

cation. Abell 2941 has also been identified as a *ROSAT* All Sky Survey (RASS) source (Voges et al. 1999) and X-ray cluster, RXCJ0145–5300 at $z = 0.1183$ by de Grandi et al. (1999).

4.1.2. *ACT-CL J0641-4949 (Abell 3402)*

Abell 3402 is included in the catalog of rich optical clusters of Abell et al. (1989) with R=0 richness. We identify its BCG (by examining the DSS images) as the 2MASS source 2MASS J06413783–4946548 (Skrutskie et al. 2006). The cluster has not been targeted spectroscopically, however, the redshift of the BCG ($z = 0.146$)
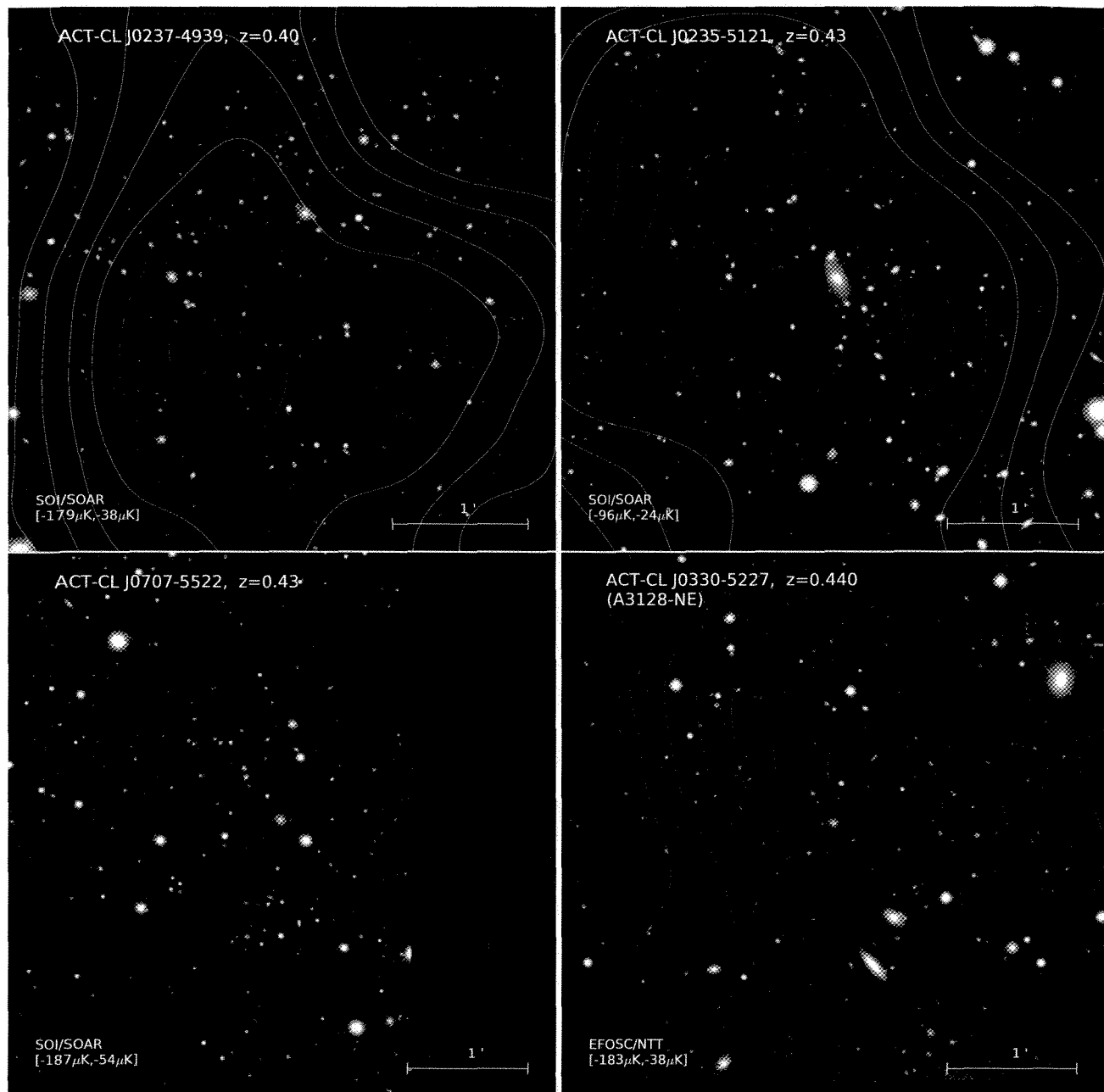
Figure 6. Composite color images for ACT-CL J0237-4939, ACT-CL J0707-5522, ACT-CL J0235-5121 and ACT-CL J0330-5227 (Abell 3128 North-East). The horizontal bar shows the scale of the images, where north is up and east is left. White contours show the 148 GHz SZE maps with the minimum and maximum levels, in μK, displayed between brackets.

has been reported as part of the 6dF survey (Jones et al. 2009). It is worth mentioning that despite its low redshift, Abell 3402 has not been reported as an X-ray source by any survey yet (including the RASS). More-over, the relatively large distance between the SZE centroid and the cluster BCG (1.8′) may suggest that this is potentially a spurious association. Note that the BCG falls right at the edge of the field of view shown in Fig. 4 (upper right panel). Further spectroscopy and X-ray observations of the cluster will provide definite information to determine whether this is a bona fide association with the SZE detection or a case of a "cluster behind a cluster"

like ACT-CL J0330−5227 (see section 4.1.8)

4.1.3. *ACT-CL J0645-5413 (Abell 3404)*

Abell 3404 was first reported by Abell et al. (1989) as an optical cluster with R=1 richness class and it was also detected as a RASS bright source (Voges et al. 1999). The cluster redshift, $z = 0.1661$, was reported by de Grandi et al. (1999) and the system is also know by its REFLEX designation RXCJ0645.4−5413 (Böhringer et al. 2004).

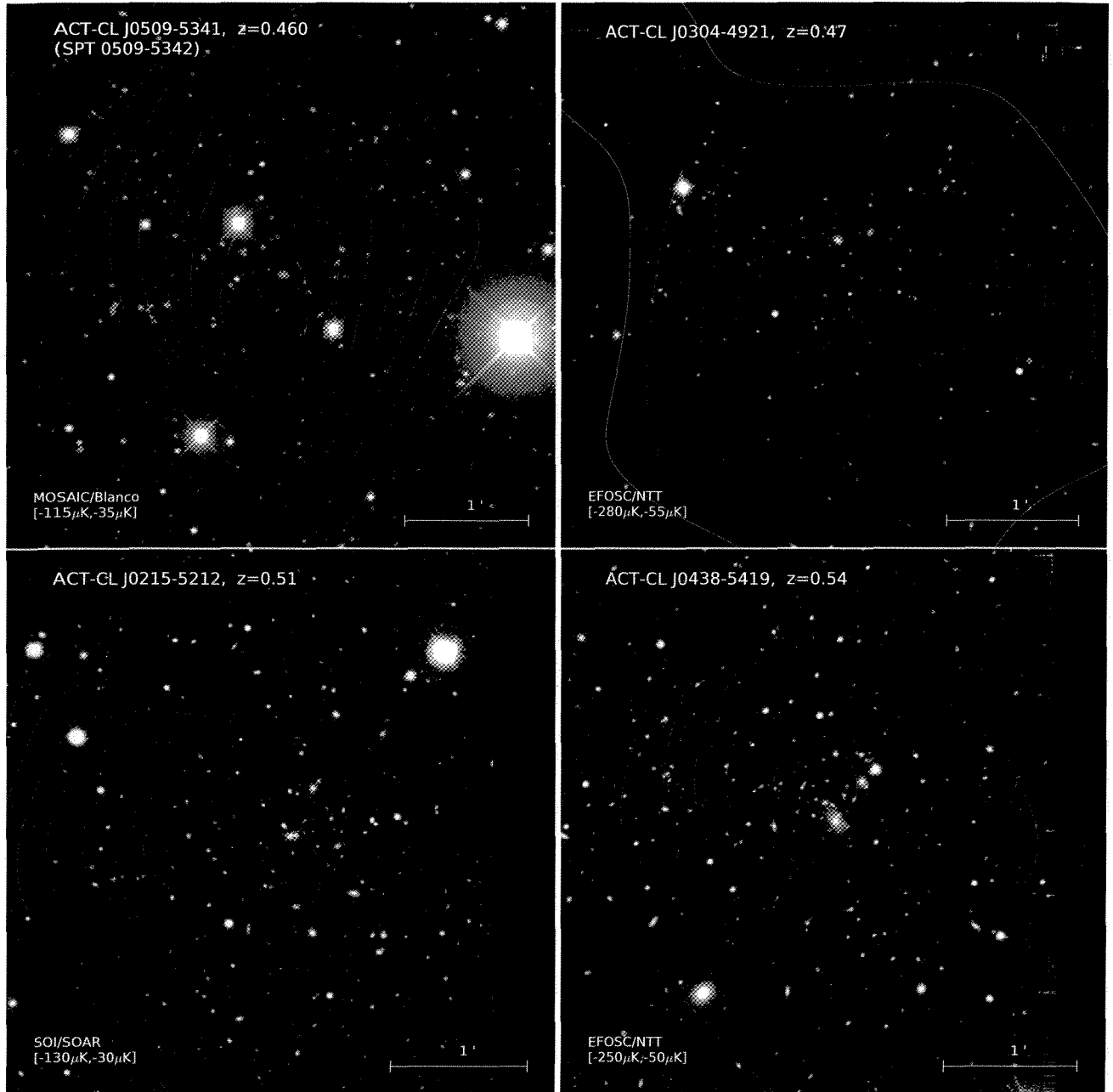### 4.1.4. *ACT-CL J0638-5358 (Abell S0592)*

Figure 7. Composite color images for ACT-CL J0509-5341 (SPT-CL J0509-5342), ACT-CL J0304-4921 , ACT-CL J0215-5212 and ACT-CL J0438-5419. The horizontal bar shows the scale of the images, where north is up and east is left. White contours show the 148 GHz SZE maps with the minimum and maximum levels, in μK, displayed between brackets.

Abell S0592 was first reported by Abell et al. (1989) in their supplementary table of southern clusters. These were clusters not rich enough or too distant to satisfy the criteria to be included in the rich nearby main cluster catalog. It was also later reported as a *ROSAT* bright source in the RASS (Voges et al. 1999) and as the REFLEX X-ray cluster, RXC J0638.7$-$5358 (Böhringer et al. 2004) at $z = 0.2216$ (de Grandi et al. 1999). Abell S0592 was first reported as an SZE source by ACT (ACT-CL J0638-5358) in Hincks et al. (2009).

4.1.5. *ACT-CL J0516-5430 (Abell S0520)*

Abell S0520 is an optically-rich cluster reported by Abell et al. (1989) in their supplementary catalog and it is located at $z = 0.294$ (Guzzo et al. 1999). It has been reported as a *ROSAT* bright source in the RASS (Voges et al. 1999) and it is known by its REFLEX designation RXCJ0516.6$-$5430 (Böhringer et al. 2004). This cluster was also detected as an SZE cluster by SPT (Staniszewski et al. 2009) and the results from several mass estimates (optical, X-ray and weak lensing) suggest a value of $M \gtrsim 5 \times 10^{14} M_\odot$ (Zhang et al. 2006; Menanteau & Hughes 2009; McInnes et al. 2009).
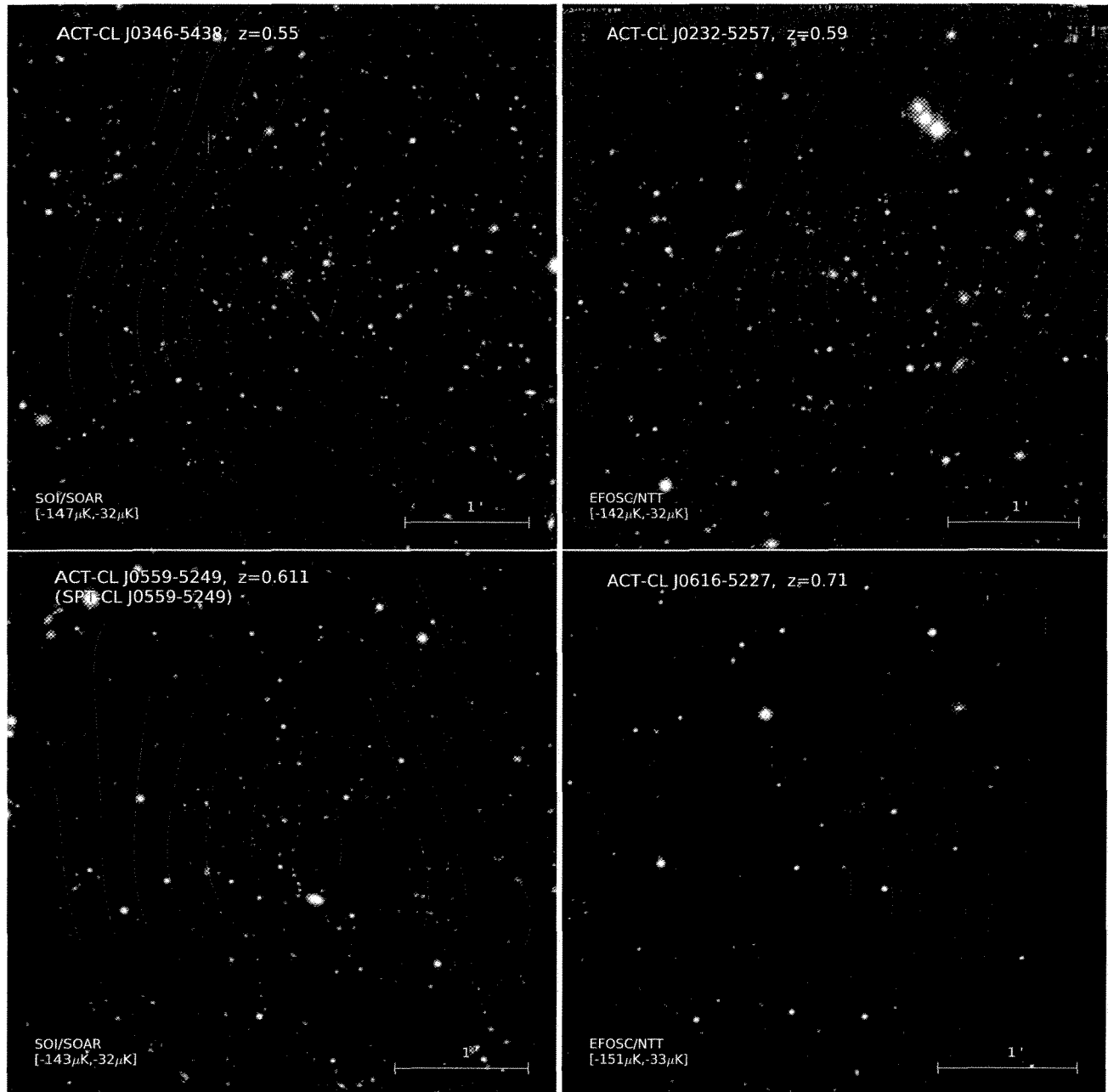
Figure 8. Composite color images for ACT-CL J0346-5438, ACT-CL J0232-5257, ACT-CL J0559-5249 (SPT-CL J0559-5249) and ACT-CL J0616-5227. The horizontal bar shows the scale of the images, where north is up and east is left. White contours show the 148 GHz SZE maps with the minimum and maximum levels, in μK, displayed between brackets.

4.1.6. ACT-CL J0245-5302 (Abell S0295)

The galaxy cluster Abell S0295 at $z = 0.300$ (Edge et al. 1994), was originally selected optically (Abell et al. 1989) and was also detected in the RASS (Voges et al. 1999). There has been a reported discovery of a giant strong-lensing arc near the brightest cluster galaxy (Edge et al. 1994), which we confirm in our imaging (see lower left panel of Figure 5). There were also previous (unsuccessful) attempts at detecting the SZE effect at 1.2-mm and 2-mm using SEST (Andreani et al. 1996). The ACT detection of this cluster is highly significant (it is ranked in the top 5 of the sample of 23). Abell S0295 was first

reported as an ACT SZE source (ACT-CL J0638-5358) by Hincks et al. (2009). *ASCA* observations yielded an average temperature of $kT = 6.72 \pm 1.09$ keV (Fukazawa et al. 2004). Figure 5 shows our deep, multicolor optical imaging of this cluster from the CTIO 4-m telescope in January 2010. The distribution of galaxies is highly elongated and matches well the shape of the SZE contours; both suggest the idea that this is a merging system.

4.1.7. ACT-CL J0217-5245 (RXC J0217.2-5244)

RXC J0217.2−5244, at $z = 0.343$, was first identified as an X-ray cluster by the REFLEX survey (Böhringer et
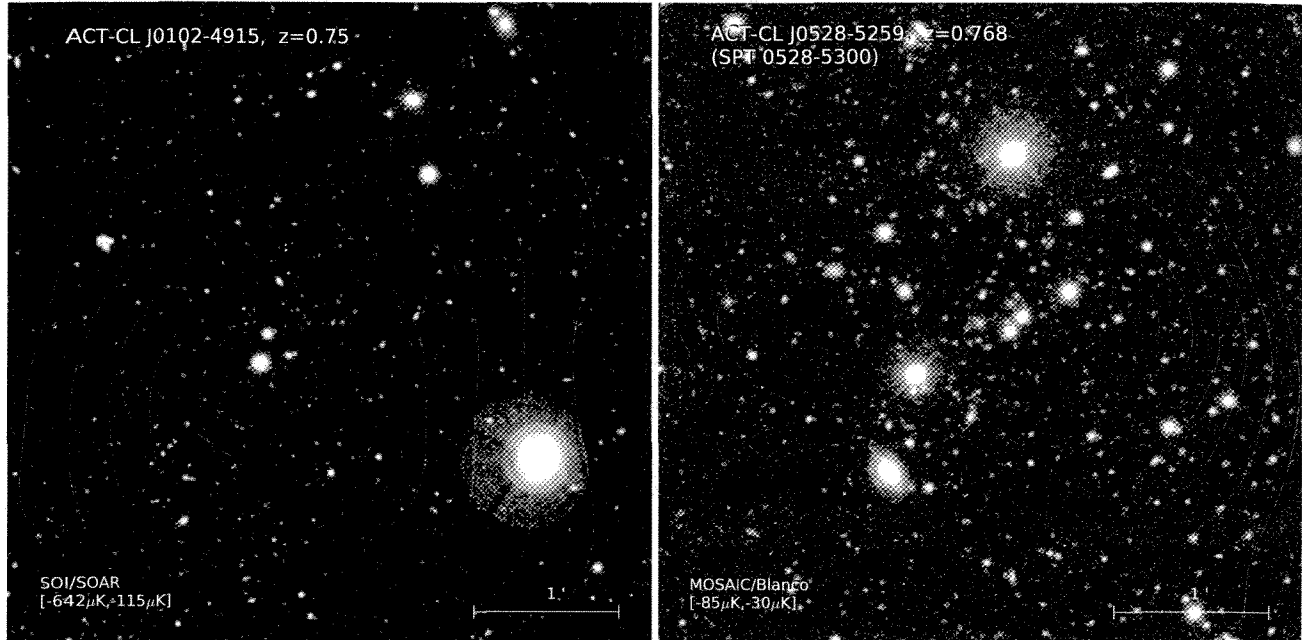
Figure 9. Composite color images for ACT-CL J0102-4915 and ACT-CL J0528-5259 (SPT-CL J0528-5300). The horizontal bar shows the scale of the images, where north is up and east is left. White contours show the 148 GHz SZE maps with the minimum and maximum levels, in μK, displayed between brackets.
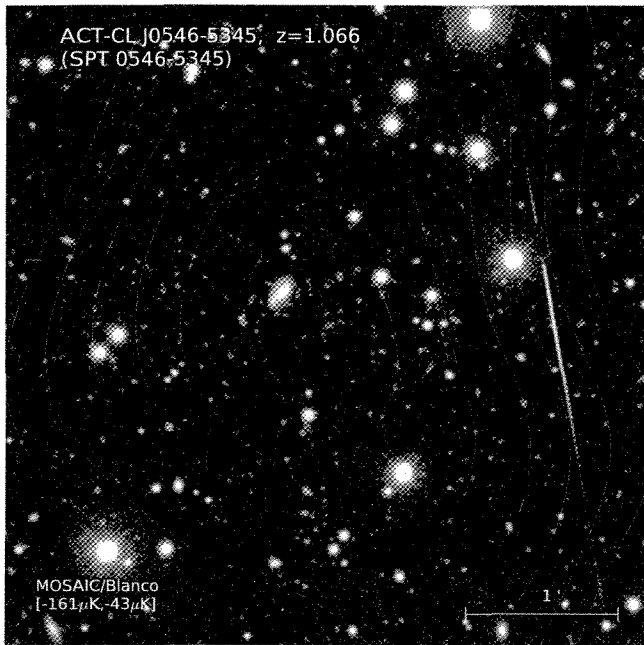

Figure 10. Composite color images for ACT-CL J0546-5345 (SPT-CL J0546-5345). The horizontal bar shows the scale of the images, where north is up and east is left. White contours show the 148 GHz SZE maps with the minimum and maximum levels, in μK, displayed between brackets.

al. 2004). Close comparison of the SUSI/NTT archival imaging with the ACT 148GHz contours (see Figure 5) shows a double-peaked morphology in the SZ maps that matches the position of the cluster BCG and the second brightest elliptical galaxy.

4.1.8. *ACT-CL J0330-5227 (Abell 3128 North-East)*

Abell 3128 North-East (NE) is a great example of the power of the SZE to detect clusters regardless of redshift and only limited by mass. Until Werner et al. (2007), using *XMM-Newton* data, revealed a more distant ($z = 0.440$) and more massive cluster superposed on the northeastern component of Abell 3128, it was believed to be part of the Horologium-Reticulum supercluster at $z = 0.06$, although its X-ray morphology is clearly double peaked with the two components separated on the sky by some 12' (Rose et al. 2002). Hincks et al. (2009) confirmed the Werner et al. (2007) results that Abell 3128 (NE) is indeed a separate higher redshift cluster, and a case of finding a cluster behind a cluster. We do not detect with ACT a significant decrement from the lower redshift southwestern component. We show our optical EFOSC/NTT imaging of the cluster in Figure 6. There is a strong lensing arc a few arcsecond southwest of the central brightest cluster galaxy.

4.1.9. *ACT-CL J0658-5557 (1ES0657-558)*

1ES0657−558 is the famous "Bullet" cluster, which we detect with the highest significance of any cluster in the ACT sample. Previous detections of the mm-band SZE signal from this cluster have been reported by ACBAR (Gomez et al. 2004), APEX-SZ (Halverson et al. 2009) and SPT (Plagge et al. 2010).

4.1.10. *Overlap with the SPT sample*

Four clusters in our sample overlap with SZE discovered systems previously reported by SPT. This presents an opportunity to compare observed clusters properties using different observing strategies and techniques (albeit sometimes the same archival data).

ACT-CL J0509−5345, ACT-CL J0547−5345 and ACT-CL J0528−5399 were first reported by Staniszewski et al. (2009) and their physical properties (photometric
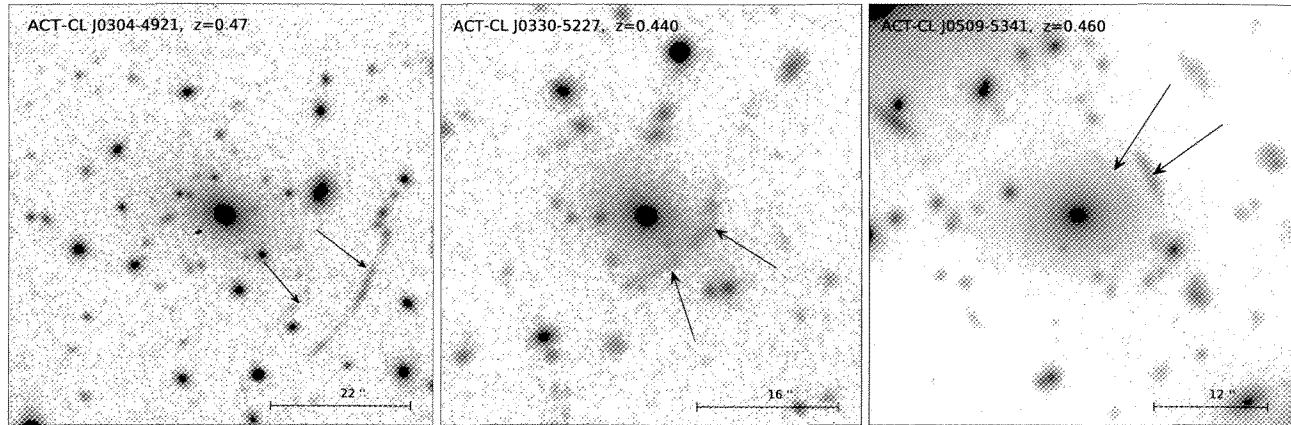
Figure 11. Close-up monochrome images of examples of strong lensing arcs in three clusters in the ACT sample.

redshifts, luminosities and mass estimates) reported in Menanteau & Hughes (2009). They have been the focus of intense multi-wavelength observations to establish their redshifts and estimate their masses using different techniques. Our team has secured multi-object spectroscopic redshifts for these systems using FORS2 on the VLT during 2009B (084.A-0577, PI:Infante) as part of a dedicated program aimed to calibrate the observable–cluster mass scaling relations of SZE clusters at high redshift (see Infante et al. 2010). Two of these systems, J0509−5345 ($z = 0.461$) and J0528−5399 ($z = 0.768$), have spectroscopic redshifts consistent with those recently reported by High et al. (2010). For ACT-CL J0547−5345 we have secured the highest spectroscopic redshift, $z = 1.0678$ for an SZE-selected clusters until now (Infante et al. 2010, Brodwin et al. 2010).

The spectroscopic redshift for ACT-CL J0559−5249, (SPT-CL J0559−5249), $z = 0.611$ has been reported by High et al. 2010 and provides a consistency check for our photometric redshift for this system, $z = 0.56 \pm 0.06$.

4.2. Gravitational lensing features

A number of the clusters in our sample show gravitational lensing features, indicative of massive systems. The excellent seeing conditions of the 2009B runs used for this study, enable us to unambiguously determine that 6 of the 23 clusters show strong lensing arcs. Three of these have already been reported in the literature: ACT-CL J0658−5557 (1E0657-56/Bullet), ACT-CL J0245−5302 (AS0295), and ACT-CL J0546−5345. Arcs in the other three are reported here for the first time: ACT-CL J0330−5227 (Abell 3128-NE), ACT-CL J0509-5341, and ACT-CL J0304−4921. In Figure 11 we show close-up monochromatic images of the clusters with newly identified strong lensing arcs in the sample.

4.3. Photometric Redshifts of the Clusters

Ten systems in our sample of ACT SZE clusters are completely new systems, for which the only optical data available are from our NTT and SOAR imaging collected during 2009B. The main objective of our observations was to confirm SZE clusters via optical identification as real systems; and in the case that observations were carried under photometric conditions — which was true for both NTT and SOAR runs — to compute crude photometric redshift estimates using the *gri* (and *z* in some

cases) imaging for the observed clusters. Therefore we can provide only photometric redshift estimates for these new systems (see Table 2). A small subsample of the targeted clusters (9) has spectroscopic information available, which we can use to perform some basic comparison between the photometric and spectroscopic redshifts. Unfortunately, the imaging of this subsample is quite heterogeneous and comes from different datasets (4 from CTIO 4-m, 3 from NTT and 2 from SOAR) making it difficult to characterize the photometric redshift errors for the sample. In Figure 12 we show the comparison between spectroscopic and photometric redshift for the mean cluster value (top panel) and the BCG (bottom panel) for the subsample of nine clusters. We calculate the mean photometric redshift for each cluster, z_{cluster}, with a procedure similat to that used in Menanteau et al. (2010). This consists of iteratively selecting cluster member galaxies using a 3σ median sigma-clipping algorithm within a local color-magnitude relation (using all available colors) defined by galaxies that: a) were photometrically classified as E or E/S0s according to their BPZ-fitted SED type, b) are within a projected radius of 500 kpc from the BCG and c) are within the redshift interval $|z - z_{\mathrm{cluster}}| = |\Delta z| = 0.05$. The uncertainty on this redshift estimate was taken to be the weighted rms of the individual galaxies chosen as members. The uncertainties associated with the BCG photometric redshifts were estimated from the BCG $p_{\mathrm{BPZ}}(z)$ function. These probability functions are non-Gaussian as revealed by the asymmetric error bars in Figure 12 (lower panel).

In Table 3 we provide the mean cluster and BCG photometric redshift estimates and associated 68% C.L. uncertanties. Despite the relatively large errors on the photometric redshifts (driven by the limited number of bands used) they are still useful for providing cosmological constraints (see Sehgal et al. 2010).

4.4. False Positive Rate

We expect fewer than 0.010 false positives based on targeting 49 regions of the sky and assuming an expected cluster number density of 0.06 deg^{-2} and a positional offset between the BCG and the SZ target centroid of $2'$. This assumes a random association with a cluster at or above the mass threshold of our sample. We would expect to find one random association for a cluster density of 5.96 deg^{-2}, which corresponds to a mass threshold of

Table 3
Cluster Photometric Redshifts

ACT Descriptor	$z_{cluster}$	z_{BCG}	z_{spec}	Tel.	Filters
ACT-CL J0232-5257	0.59 ± 0.07	$0.59^{+0.56}_{-0.63}$	$\cdots$	EFOSC/NTT	g, r, i
ACT-CL J0304-4921	0.47 ± 0.05	$0.42^{+0.41}_{-0.51}$	$\cdots$	EFOSC/NTT	g, r, i
ACT-CL J0330-5227	0.52 ± 0.07	$0.48^{+0.42}_{-0.59}$	0.440	EFOSC/NTT	g, r, i
ACT-CL J0438-5419	0.54 ± 0.05	$0.54^{+0.44}_{-0.56}$	$\cdots$	EFOSC/NTT	g, r, i
ACT-CL J0616-5227	0.71 ± 0.10	$0.71^{+0.67}_{-0.78}$	$\cdots$	EFOSC/NTT	g, r, i
ACT-CL J0641-4949	0.18 ± 0.07	$0.16^{+0.14}_{-0.21}$	0.146	EFOSC/NTT	g, r, i
ACT-CL J0645-5413	0.19 ± 0.04	$0.19^{+0.16}_{-0.22}$	0.167	EFOSC/NTT	g, r, i
ACT-CL J0102-4915	0.75 ± 0.04	$0.78^{+0.76}_{-0.81}$	$\cdots$	SOI/SOAR	g, r, i, z
ACT-CL J0145-5301	0.12 ± 0.06	$0.13^{+0.11}_{-0.18}$	0.118	SOI/SOAR	g, r, i
ACT-CL J0215-5212	0.51 ± 0.05	$0.52^{+0.50}_{-0.55}$	$\cdots$	SOI/SOAR	g, r, i
ACT-CL J0235-5121	0.43 ± 0.06	$0.42^{+0.31}_{-0.49}$	$\cdots$	SOI/SOAR	g, r, i
ACT-CL J0237-4939	0.40 ± 0.05	$0.36^{+0.35}_{-0.43}$	$\cdots$	SOI/SOAR	g, r, i
ACT-CL J0346-5438	0.55 ± 0.05	$0.58^{+0.54}_{-0.64}$	$\cdots$	SOI/SOAR	g, r, i
ACT-CL J0559-5249	0.56 ± 0.06	$0.56^{+0.55}_{-0.64}$	0.611	SOI/SOAR	g, r, i, z
ACT-CL J0707-5522	0.43 ± 0.07	$0.44^{+0.33}_{-0.52}$	$\cdots$	SOI/SOAR	g, r, i
ACT-CL J0509-5341	0.36 ± 0.13	$0.35^{+0.35}_{-0.50}$	0.461	MOSAIC/Blanco	g, r, i
ACT-CL J0516-5430	0.25 ± 0.08	$0.26^{+0.26}_{-0.47}$	0.294	MOSAIC/Blanco	g, r, i
ACT-CL J0528-5259	0.69 ± 0.05	$0.69^{+0.67}_{-0.72}$	0.768	MOSAIC/Blanco	g, r, i
ACT-CL J0546-5345	0.93 ± 0.13	$0.95^{+0.89}_{-1.04}$	1.066	MOSAIC/Blanco	g, r, i

$1.7 \times 10^{14} M_\odot$ assuming a distribution of massive haloes using the Tinker et al. (2008) mass function. Abell 3402 might be in this situation, which would explain the large positional offset between its BCG and peak SZ decrement and its lack of significant X-ray emission.

4.5. *The Purity of the Sample*

The extraction methodology of SZE cluster candidates evolved during the 2009B season and as a result the candidates observed in the first run (at the NTT) came from a list of targets that was later revised once the selection method was more stable (see Section 3.1). The revised sample for our second run (at SOAR) in December 2009 contained all of the high signal detections observed on the NTT run. This later list, from which we targeted 49 systems, is therefore the most uniformly observed as a function of signal-to-noise and the one best suited to estimate the purity of SZE candidates. We utilized the Blanco archival data in the 05hr field to supplement our NTT and SOAR imaging, although no new clusters were found (beyond those previously found by SPT). By purity here we mean the ratio of optically-confirmed clusters to SZE detections. In Figure 13 we show the purity from the sample of 49 targeted systems as a function of signal-to-noise as the thick and thin solid line types (these correspond to different event binning). Since we did not observe every cluster candidate at signal-to-noise ratios below 5, for reference we also show, using dashed lines, the fraction of candidates greater than a given signal-to-noise that were actually imaged in this program.

We achieve 100% purity for signal-to-noise ratios greater than 5.7 where there are 10 clusters. This drops to a purity value of 80% for a SNR of 5.1. We targeted all of the SZ candidates down to a signal-to-noise of 4.8 and for this sample the purity is 71% (17/24). Below this SNR value the purity of the SZ candidates drops sharply. Only six clusters were optically confirmed out of

25 candidates targeted (24% purity) over the SNR range 4.2–4.8. However, as we were unable to target all of the SZ candidates in this SNR range, assigning a precise estimation of the purity is not possible. Another estimate for the purity comes from conservatively assuming that none of the untargeted SZE candidates is a real system, in which case the overall purity would be $\simeq$ 9% in the signal-to-noise ratio range between 4.2 and 4.8.

An important conclusion of this analysis is that within our high SNR sample (>5.7), which was fully observed, we report no clusters above a redshift of 1.1. As we show next, this distribution is fully consistent with expectations of ΛCDM which are based on Gaussian fluctuations in the primordial matter density distribution. Deviations from Gaussianity can perturb the expected number of massive clusters at high redshift. Thus the large area surveyed by ACT and the well-established redshift distribution of the sample, can be used to put important constraints on the level of non-Gaussianity, defined by the dimensionless coupling parameter, f_{NL} (see Komatsu & Spergel 2001; Lo Verde et al. 2008). This will be the focus of a future study.

4.6. *Mass Threshold of the Cluster Sample*

Here we describe how we estimate the approximate mass limit of the observed sample. We binned the number of clusters as a function of redshift in bins of $\Delta z = 0.2$ and fitted to the redshift distribution of massive haloes using the Tinker et al. (2008) mass function and cosmological parameters from Komatsu et al. (2009), assuming that all (no) clusters above (below) the threshold were detected. The number counts were assumed to be Poisson-distributed in each bin and the appropriate likelihood function was calculated and used as the figure-of-merit function for the fits. In Figure 14 we show the cumulative number distribution of optically-confirmed ACT SZ clusters (the histograms) per square
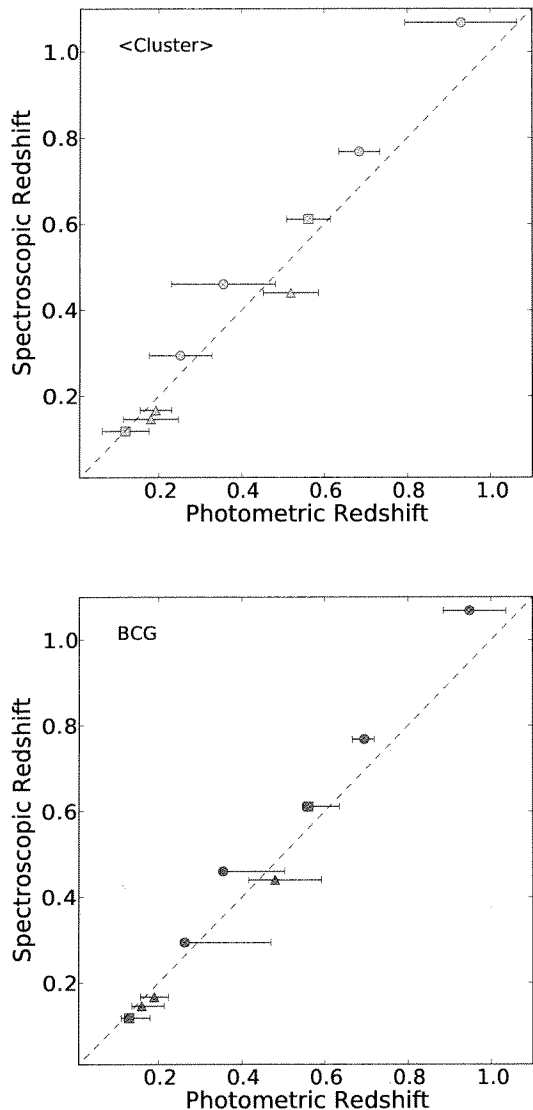
Figure 12. Spectroscopic redshift versus photometric redshift for the sub sample of 8 ACT clusters with known redshifts. Circles, triangles and squares represent imaging data from the MOSAIC/Blanco, EFOSC/NTT and SOI/SOAR telescopes. Error bars represent 68% C.L. uncertainties on the cluster photometric redshift.

degree as a function of redshift. We make two assumptions here: a) that the area surveyed is 455 deg^2 even though all of this was not covered to the same depth, and b) that the sample is complete out to a redshift of 1.2. The upper histogram is for the entire sample of clusters from Table 2, while the bottom histogram is for the subset of clusters above a SNR of 5.7 which has 100% purity. We overplot curves that give the expected distribution for different mass thresholds based on structure formation in a ΛCDM model (Tinker et al. 2008). The full sample of 23 is well characterized by a mass threshold of $8 \times 10^{14} M_\odot$ and the 10 highest significance clusters, where all ACT SZ candidate clusters were optically confirmed, are consistent with a mass threshold
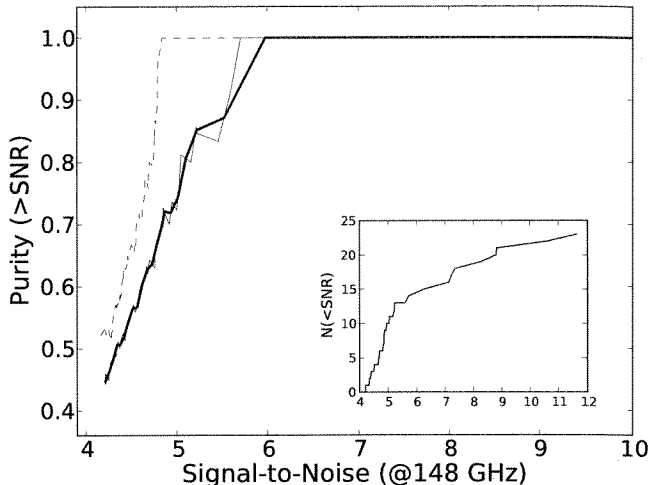

Figure 13. The SZE sample purity greater than a given SNR in the ACT 148 GHz maps. The purity is defined as the ratio of the number of confirmed clusters to the number of observed clusters. The thick solid line represents the purity binned in n=2 events, while the thin line represents no binning. The dashed line represent the fraction of candidates from the sample greater than a given SNR that were actually observed. The inset plot shows the cluster cumulative distribution as a function of SNR for the optically-confirmed cluster sample.
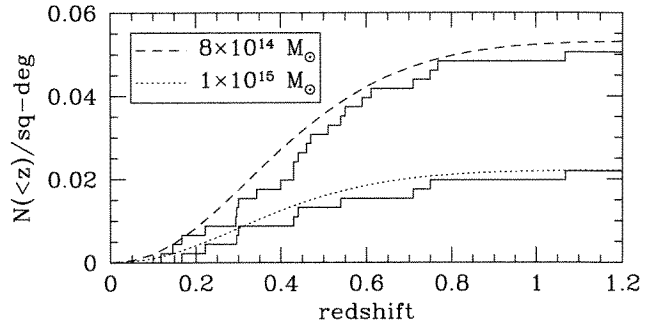

Figure 14. Cumulative distribution of ACT SZE clusters per square degree as a function of redshift. The top histogram is for the full sample of 23 clusters; the bottom one is for the high significance subsample of 10 clusters. The curves show the best fit model distributions for each.

of $1 \times 10^{15} M_\odot$. These mass thresholds are in agreement with their X-ray luminosities (Fig. 15) and with simulations given the current ACT survey noise (Sehgal et al. 2010). Thus there is consistency between the SZ, optical, and X-ray observations with the model. Note that if the actual area were significantly smaller than 455 deg^2 or clusters were missed, the mass thresholds would decrease. Therefore the mass threshold values quoted here can be considered strong upper limits.

4.7. Unconfirmed High Signal-to-Noise Candidates

Beyond the reported sample of 23 clusters (Table 2), there are in addition three SZE cluster candidates (not reported) at relatively high SNR (>5.1) for which we do not find an optical counterpart using the procedure described above. One of these we observed at the NTT and then again for twice as long at SOAR, where we

also included the z-band. Although there are potential BCGs in the field of view (based on our low accuracy photometric redshifts), none is accompanied by a red sequence containing more than $\simeq 15$ galaxies within a projected radius of 500 kpc. This value is consistent with the average surface density of galaxies at $z \simeq 1$ and additionally is far below the typical observed richness of the confirmed clusters ($\simeq 60$ members) in the optical. Thus we can confidently conclude that these three candidates are not optical clusters in the redshift range $z \lesssim 1.2$ with optical properties like those of the confirmed sample (Table 2). An obvious possibility is that these are high redshift clusters, beyond the reach of our observational program. However, for the Tinker et al. (2008) distribution of massive haloes in the ΛCDM cosmology, we expect only 0.6 or 0.1 clusters (for $M = 6$ and $8 \times 10^{14} M_\odot$, respectively) beyond a redshift of 1.2 over the area surveyed. Future near-IR or warm phase *Spitzer* IRAC imaging is required to determine whether these are high-redshift massive clusters.

5. CLUSTER X-RAY PROPERTIES

In order to estimate masses we turn to X-ray observations, using archival datasets from *ROSAT*, *Chandra* and *XMM-Newton*, and measure X-ray luminosities to serve as coarse mass proxies. Here we describe the X-ray data reduction and analysis and present the X-ray properties of the ACT clusters.

5.1. *ROSAT Observations*

We searched for X-ray counterparts to the ACT clusters using the RASS data following the same procedure as in Menanteau & Hughes (2009). The raw X-ray photon event lists and exposure maps were downloaded from the MPE *ROSAT* Archive[29] and were queried with our own custom software. At the position of each cluster, RASS count rates in the $0.5 - 2$ keV band (corresponding to PI channels 52–201) were extracted from within radii of $3'$ to $9'$ (chosen appropriately for each cluster) for the source emission and from within a surrounding annulus ($12'$ to $30'$ inner and outer radii) for the background emission. Obvious point sources were excluded from both source and background regions. The background-subtracted count rates were converted to X-ray luminosity (in the 0.1–2.4 keV band) assuming a thermal spectrum ($kT = 5$ keV) and the Galactic column density of neutral hydrogen appropriate to the source position, using data from the Leiden/Argentine/HI Bonn survey (Kalberla et al. 2005). In Table 4 we show the X-ray fluxes and luminosities for all ACT clusters, regardless of the significance of the RASS detection.

5.2. *Chandra Observations*

All available archival *Chandra* data for clusters in our sample are used in this analysis. The combined exposure times of the observations for each cluster are shown in Table 5. Data are reduced using CIAO version 4.2 and calibration data base version 4.2.0. The data are processed starting with the level 1 events data, removing the cosmic ray afterglow correction, and generating a new bad pixel file that accounts for hot pixels and cosmic ray

---

[29] ftp://ftp.xray.mpe.mpg.de/rosat/archive/

afterglows. Using the newly generated bad pixel file, the charge transfer inefficiency correction, time-dependent gain adjustment, and other standard corrections are applied to the data. The data are filtered for *ASCA* grades 0, 2, 3, 4, 6 and status=0 events and the good time interval data provided with the observations are applied. Periods of high background count rate are excised using an iterative procedure involving creating light curves in background regions with 259 s bins (following the ACIS "Blank-Sky" Background File reduction), and excising time intervals that are in excess of 3 σ (=rms) from the mean background count rate. This sigma clipping procedure is iterated until all remaining data lie within 3 σ of the mean. All observations are in the ACIS-I configuration and background regions are chosen among the chips free from cluster emission, at approximately the same distance from the readout as the cluster. This is to account for a gradient in the front-illuminated chip response seen when investigating deep blank-sky exposures (Bonamente et al. 2004).

Images are created by binning the data by a factor of four, resulting in a pixel size of $1.97''$. Exposure maps are constructed for each observation at an energy of 1 keV. Images and exposure maps are combined in cases where there are multiple observations of the same cluster. A wavelet-based source detector is used on the combined images and exposure maps to generate a list of potential point sources. The list is examined by eye, removing bogus or suspect detections, and then used as the basis for our point source mask.

Spectra are extracted in regions that are 3σ above the background level, where σ is the uncertainty in the background measurement. Surface brightness profiles are constructed using $5''$ bins and are used to estimate the background surface brightness and the uncertainty in the background. The radius corresponding to 3σ above the background, $\theta_{3\sigma}$, is computed and used for the spectral extraction, accounting for the point source mask. Spectra are extracted and responses calculated for each individual observation. All of the spectra for a given cluster are then fit simultaneously.

ACIS quiescent backgrounds are used to construct background spectra for each of the observations. Appropriate quiescent background files are reprojected to match each observation and background spectra are extracted in the same $\theta_{3\sigma}$ regions used for the cluster spectra. The background spectra are then normalized to match the count rate of the cluster spectra in the 9.5–12.0 keV range, where the *Chandra* response is negligable and the particle background dominates (e.g., Vikhlinin et al. 2005).

XSPEC (Arnaud 1996) is used to fit the X-ray spectrum assuming a thermal plasma emission model (using the so-called "Mekal" model; Mewe et al. 1985), multiplied by a Galactic absorption model, with solar abundances of Asplund et al. (2009) and cross sections of Balucinska-Church & McCammon (1992) including an updated He cross section (Yan et al. 1998). For the absorption component we fixed the column density of neutral hydrogen to the Galactic value toward the cluster position (obtained in the same way as for the RASS data). Spectra are grouped such that there are a minimum of 20 counts per bin and the χ^2 statistic is used for the fit. All spectra for a given cluster are fit simultaneously to the
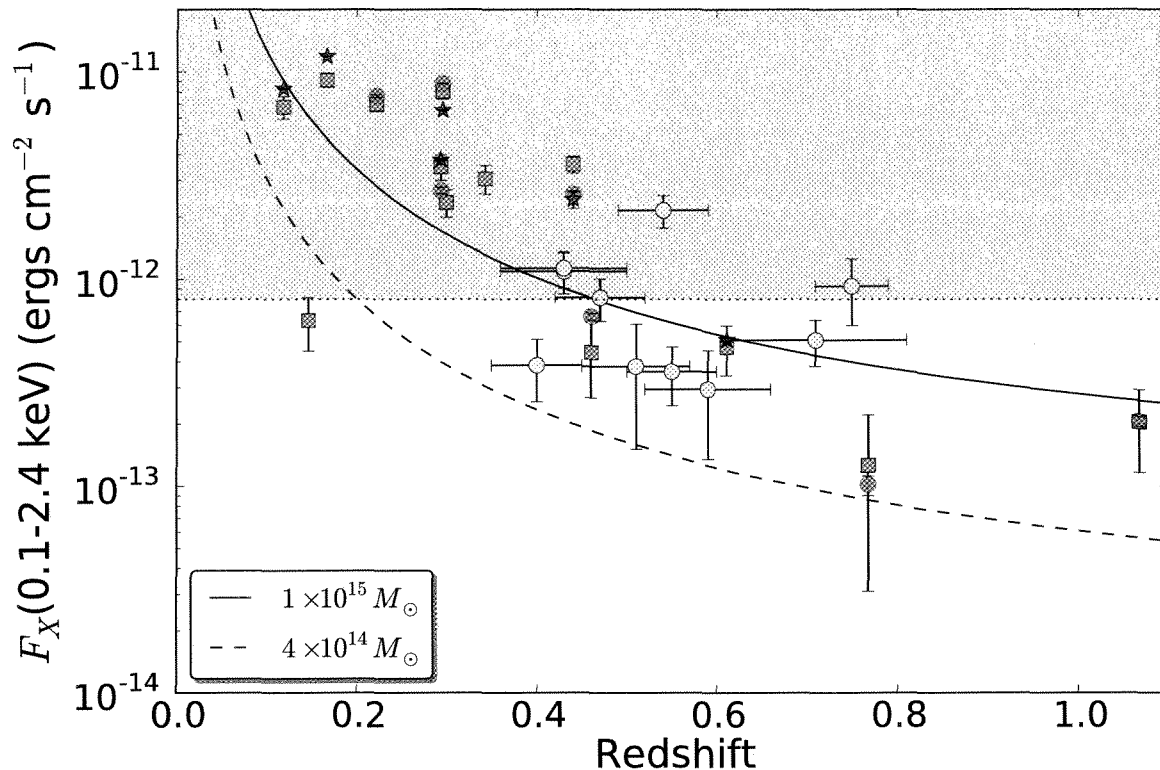
Figure 15. The soft X-ray flux (in the observed band of 0.1–2.4 keV) as a function of redshift for ACT SZE-selected clusters. The filled squares are known clusters and the open circles are RASS fluxes for seven new ACT clusters with only photometric redshifts. Red circles and blue stars represent flux values from *Chandra* and *XMM-Newton* observations respectively. The solid and dashed curves represent the expected X-ray fluxes for clusters with masses $M_{200} = 4 \times 10^{14}\, M_\odot$ and $1 \times 10^{15}\, M_\odot$, respectively, using scaling relations from Vikhlinin et al. (2009). The gray area at the top corresponds approximately to the regime of the RASS bright source catalog (Voges et al. 1999).

same plasma model, including linking the normalizations between data sets. The fit is limited to photons within the energy range 0.3-9.0 keV. To estimate fluxes in the 0.1-2.4 keV *ROSAT* band, the energy range is extended below *Chandra*'s nominal energy range. Fluxes, F_X, and luminosities, L_X, in the 0.1-2.4 keV band are then computed from the best fit model. Uncertainties in the fluxes and luminosities are estimated by varying the temperature, T_e, abundance, Z, and normalization of the model using the extremities of the 68% confidence regions for the parameters. The results are summarized in Table 5, which shows the redshift (z), total effective exposure time (t_{exp}), column density (N_H), the spectral extraction radius in angular ($\theta_{3\sigma}$) and physical ($R_{3\sigma}$) units, spectral parameters from the fit (T_e and Z), and the resulting flux and luminosity (F_X and L_X) for each cluster.

5.3. *XMM-Newton Observations*

For the *XMM-Newton* observations we started with the pipeline-processed data supplied as part of the standard processing. A combined background-subtracted and exposure-corrected image was created for each cluster in the 0.5–2 keV band by merging data from the three EPIC cameras: PN, MOS1 and MOS2. These were used to define the optimal radii for spectral extraction, initially taken as the radius where the estimated cluster emission fell below the background level. These source

regions were further refined by increasing the extraction radii by factors of 10% until the extracted flux values converged to an accuracy of a few percent. The regions, in nearly all cases, were elliptical. Background spectra came from a surrounding annular region with sufficient area to obtain good photon statistics. Event lists were filtered to remove time periods of high count rate background flares and to include only good event patterns ($\le$ 12 for MOS and $\le$ 4 for the PN). Other standard filters to remove bad pixels and chip edges, for example, were applied. We used standard *XMM-Newton* software tools to calculate the instrumental response functions for each cluster (treating the data from each camera independently). The cluster image itself was used for the weighting to generate the response functions. The same absorbed thermal plasma model as described above was used to fit the PN, MOS1, and MOS2 data, again using XSPEC. The individual spectral data sets were fitted separately with linked parameters. X-ray fluxes and luminosities were determined using the best-fitted spectrum. The uncertainties on these include the 1σ range on temperature and overall normalization. Results are given in Table 6.

5.4. *Summary of X-ray Properties*

The soft X-ray fluxes as a function of redshift are shown in Figure 15. We plot all datasets: RASS in gray, *Chan-*

Table 4
ROSAT Cluster Properties

ACT Descriptor	z	t_{exp} (s)	N_H $(10^{20}$ cm$^{-2})$	θ (arcmin)	R $(h_{70}^{-1}$ kpc)	F_X [a] (0.1−2.4 keV)	L_X [b] (0.1−2.4 keV)
ACT-CL-J0145-5301	0.118	247	2.67	9.0	1151	67.59 ± 8.39	2.30 ± 0.29
ACT-CL-J0641-4949	0.146	859	3.37	6.0	920	6.32 ± 1.82	0.34 ± 0.10
ACT-CL-J0645-5413	0.167	496	5.60	9.0	1542	91.17 ± 7.02	6.48 ± 0.50
ACT-CL-J0638-5358	0.222	834	6.06	8.0	1717	69.57 ± 4.74	9.13 ± 0.62
ACT-CL-J0516-5430	0.294	380	2.05	7.0	1844	34.83 ± 4.90	8.43 ± 1.19
ACT-CL-J0658-5557	0.296	470	4.90	7.0	1853	80.26 ± 6.53	19.72 ± 1.61
ACT-CL-J0245-5302	0.300	621	3.15	7.0	1870	23.39 ± 3.54	5.92 ± 0.90
ACT-CL-J0217-5245	0.343	357	2.68	7.0	2047	30.56 ± 4.86	10.40 ± 1.65
ACT-CL-J0237-4939	0.40	778	2.55	3.5	1128	3.84 ± 1.28	1.84 ± 0.61
ACT-CL-J0235-5121	0.43	460	3.03	3.5	1178	10.91 ± 2.44	6.14 ± 1.37
ACT-CL-J0707-5522	0.43	620	6.37	3.5	1178	11.29 ± 2.28	6.36 ± 1.28
ACT-CL-J0330-5227	0.440	746	1.44	6.0	2046	35.77 ± 3.35	21.20 ± 1.98
ACT-CL-J0509-5341	0.461	418	1.46	3.5	1224	4.43 ± 1.76	2.90 ± 1.15
ACT-CL-J0304-4921	0.47	699	1.77	5.0	1770	8.15 ± 1.89	5.61 ± 1.30
ACT-CL-J0215-5212	0.51	369	2.49	5.0	1850	3.79 ± 2.28	3.13 ± 1.88
ACT-CL-J0438-5419	0.54	308	1.02	3.5	1334	21.48 ± 3.83	20.21 ± 3.60
ACT-CL-J0346-5438	0.55	774	1.44	3.0	1154	3.58 ± 1.13	3.52 ± 1.11
ACT-CL-J0232-5257	0.59	425	2.84	3.5	1393	2.94 ± 1.59	3.39 ± 1.83
ACT-CL-J0559-5249	0.611	995	5.06	4.0	1618	4.69 ± 1.27	5.85 ± 1.58
ACT-CL-J0616-5227	0.71	1223	4.24	4.0	1724	5.08 ± 1.28	8.92 ± 2.24
ACT-CL-J0102-4915	0.75	227	1.72	4.0	1761	9.25 ± 3.27	18.39 ± 6.49
ACT-CL-J0528-5259	0.768	718	3.24	3.0	1332	1.26 ± 0.95	2.64 ± 2.00
ACT-CL-J0546-5345	1.066	1092	6.78	3.0	1462	2.04 ± 0.88	9.14 ± 3.94

[a] Units are $\times 10^{-13}$ erg s^{-1} cm^{-2}.
[b] Units are $\times 10^{44}$ erg s^{-1}.

dra in red, and *XMM-Newton* in blue. We indicate the region (at the high-end flux) that approximately corresponds to the flux limit of the RASS bright source catalog (Voges et al. 1999). In cases of multiple X-ray datasets the agreement among the observed fluxes is good, with the possible exception of ACT-CL-J0330-5227, where the emission from the foreground cluster contaminates the RASS flux estimate.

For reference we show curves of the expected (observed-frame) X-ray fluxes for clusters with assumed masses of $M_{200} = 4 \times 10^{14} M_\odot$ (dashed) and $1 \times 10^{15} M_\odot$ (solid) using the X-ray luminosity versus mass scaling relation in Vikhlinin et al. (2009). We use their eqn. 22, which includes an empirically determined redshift evolution. We convert their X-ray band (emitted: 0.5–2 keV band) to ours (observed: 0.1–2.4 keV) assuming a thermal spectrum at the estimated cluster temperature determined using the mass-temperature relation also from Vikhlinin et al. (2009). This too has a redshift dependence, so the estimated temperatures vary in the ranges 2.9–5.0 keV and 5.2–9.0 keV over $0.0 < z < 1.1$ for the two mass values we plot. We use conversion factors assuming the redshift-averaged temperatures of 4 keV and 7 keV, since the difference in conversion factor over the temperature ranges is only a few percent, negligible on the scale of Figure 15. The mass values in Vikhlinin et al. (2009) are defined with respect to an overdensity of 500 times the *critical* density of the Universe at the cluster redshift, while in this paper we define cluster masses with respect to an overdensity of 200 times the *average* density at the cluster redshift. We calculate the conversion factor assuming an NFW halo mass profile with the power-law relation between concentration and mass determined by Duffy et al. (2008) from large cosmological N-body simulations. This mass conversion factor is approximately 1.8 averaged over redshift, varies from 2.2

to 1.7 over $0.0 < z < 1.1$, and depends only weakly on cluster mass (few percent) for the 2 values plotted here.

The X-ray fluxes of the ACT SZE-selected clusters scatter about the $1 \times 10^{15} M_\odot$ curve, validating the mass threshold we estimated above from the cluster number counts. The most extreme outlier (on the low flux side) is Abell 3402, indicating a considerably lower mass for this system, assuming (as we have) that the SZE candidate is at the redshift of Abell 3402. For those clusters with archival *Chandra* or *XMM-Newton* data our measured temperatures are typically high $kT > 5$ keV and in good agreement with results from the recent SPT cluster X-ray analysis (Andersson et al. 2010). The masses inferred from the X-ray temperatures are consistent with the mass curves shown in Figure 15.

6. CONCLUSIONS

After many years of intense effort, we have presented the first optically-confirmed sample of 23 SZE-selected clusters of galaxies from ACT over a cosmologically significant volume. Using a combination of archival and targeted multi-color observations using 4-m telescopes we have confirmed the presence of a BCG and a rich red sequence of galaxies in 14 new SZE clusters (4 overlapping with previous ACT and SPT detections), of which 10 are presented here for the first time. Using a careful selection method of SZE candidates combined with the results from our observations we have determined the purity of the ACT SZE sample to be 100% for SNR > 5.7, 80% for SNR > 5.1, and 71% for SNR > 4.8. For lower SNR values we did not target all SZE candidates; still it is clear that the purity of the lower significance candidates has fallen substantially to between $\simeq 9\%$ and 24%.

By comparing the number distribution of clusters of galaxies as a function of redshift with the expectations from ΛCDM simulation, we estimate a typical lower mass limit of $8.0 \times 10^{14} M_\odot$ for our full sample of 23. Our

Table 5
Chandra Cluster Properties

ACT Descriptor	z	t_{exp} (ks)	N_H (10^{20} cm^{-2})	$\theta_{3\sigma}$ (arcmin)	$R_{3\sigma}$ (h_{70}^{-1} kpc)	T_e (keV)	Z ($Z_\odot$)	F_X[a] (0.1−2.4 keV)	L_X[b] (0.1−2.4 keV)
ACT-CL J0638-5358	0.222	19.9	6.06	5.20	1116	$8.51^{+0.36}_{-0.34}$	$0.46^{+0.09}_{-0.09}$	$76.64^{+1.02}_{-1.02}$	$9.87^{+0.13}_{-0.13}$
ACT-CL J0516-5430	0.294	9.5	2.05	4.05	1068	$9.59^{+1.35}_{-1.05}$	$0.49^{+0.25}_{-0.24}$	$26.79^{+1.00}_{-0.93}$	$6.30^{+0.23}_{-0.22}$
ACT-CL J0658-5557	0.296	589.4	4.90	5.92	1568	$13.56^{+0.14}_{-0.14}$	$0.36^{+0.02}_{-0.02}$	$87.75^{+0.22}_{-0.22}$	$20.69^{+0.05}_{-0.05}$
ACT-CL J0330-5227	0.440	19.3	1.44	3.60	1229	$4.32^{+0.21}_{-0.19}$	$0.11^{+0.07}_{-0.07}$	$25.72^{+0.62}_{-0.60}$	$15.50^{+0.37}_{-0.36}$
ACT-CL J0509-5341	0.460	28.8	1.46	1.95	683	$9.39^{+1.43}_{-1.07}$	$0.35^{+0.22}_{-0.23}$	$6.61^{+0.26}_{-0.24}$	$4.14^{+0.16}_{-0.15}$
ACT-CL J0528-5259	0.768	27.2	3.24	1.04	463	$4.67^{+1.45}_{-0.99}$	0.30	$1.02^{+0.12}_{-0.10}$	$2.15^{+0.24}_{-0.22}$
ACT-CL J0546-5345	1.068	57.1	6.78	1.24	605	$8.54^{+1.38}_{-1.05}$	$0.33^{+0.29}_{-0.29}$	$2.06^{+0.12}_{-0.11}$	$8.43^{+0.47}_{-0.44}$

[a] Units are $\times 10^{-13}$ erg s^{-1} cm^{-2}.
[b] Units are $\times 10^{44}$ erg s^{-1}.

Table 6
XMM-Newton Cluster Properties

ACT Descriptor	z	$t_{exp}^{MOS}, t_{exp}^{PN}$[a] (ks)	N_H (10^{20} cm^{-2})	$\theta_{minor}, \theta_{major}$ (arcmin)	R_{mean}[b] (h_{70}^{-1} kpc)	T_e (keV)	Z ($Z_\odot$)	F_X[c] (0.1−2.4 keV)	L_X[d] (0.1−2.4 keV)
ACT-CL J0145-5301	0.118	37,22	2.67	6.5,10.8	1031	5.60 ± 0.08	0.30 ± 0.02	82.96 ± 0.52	2.83 ± 0.02
ACT-CL J0645-5413	0.167	44,28	5.60	5.4,8.9	1188	7.49 ± 0.09	0.24 ± 0.01	118.70 ± 0.40	8.36 ± 0.03
ACT-CL J0516-5430	0.294	11,8	2.05	6.2,8.0	1856	7.44 ± 0.38	0.21 ± 0.05	37.57 ± 0.47	8.93 ± 0.11
ACT-CL J0658-5557	0.296	33,21	4.90	3.9,5.1	1181	10.80 ± 0.22	0.22 ± 0.03	65.22 ± 0.39	15.51 ± 0.09
ACT-CL J0330-5227	0.440	71,57	1.44	4.0,4.0	1365	5.46 ± 0.27	0.30	24.28 ± 2.34	14.60 ± 1.40
ACT-CL J0559-5249	0.611	20,14	5.06	2.0,3.5	1070	8.09 ± 0.75	0.30	5.10 ± 0.10	6.06 ± 0.12

[a] The quoted MOS exposure time is the average of the two MOS cameras.
[b] Geometric mean of the major and minor axes.
[c] Units are $\times 10^{-13}$ erg s^{-1} cm^{-2}.
[d] Units are $\times 10^{44}$ erg s^{-1}.

highest significance subsample of 10 ACT SZE cluster candidates (above a SNR of 5.7) were all confirmed optically is consistent with a mass threshold of $1.0 \times 10^{15}\ M_\odot$. We present the results of analysis of archival X-ray data from *ROSAT*, *Chandra*, and *XMM-Newton*. The X-ray data yield uniformly high temperatures ($kT \simeq 7 - 17$ keV) and luminosities ($L_X \simeq 10^{44} - 10^{45}$ erg s^{-1}), which are broadly consistent with the mass thresholds inferred from the cluster number counts as a function of redshift. Further work on measuring cluster masses using X-ray data and other techniques (e.g., galaxy dynamics and weak lensing) is underway.

While the ΛCDM model predicts that there should be very few clusters with masses greater than $8 \times 10^{14}\ M_\odot$ at $z > 1.2$, (i.e., 0.1 clusters with our current area and mass limit or 0.4% of the sample) early dark energy models (Bartelmann et al. 2006; Alam et al. 2010) and models with significant primordial non-Gaussianity (Cayón et al. 2010) predict significantly more high redshift clusters. Moreover, in quintessence models, the number of high redshift clusters is also a sensitive function of w, the dark energy equation of state (Alimi et al. 2010). Therefore, the detection of even a single massive high redshift cluster would challenge our current standard paradigm. However our ability to investigate this question here is constrained somewhat by the upper redshift limit set by the depth of our optical program. Future follow-up IR observations of high significance SZE candidates that are currently undetected in our optical imaging can probe the existence of $z > 1.2$ massive systems and provide a simple yet powerful test of ΛCDM. Even in the event of a null result (i.e., none of the high significance SZE decrements turns out to contain a cluster), the ACT cluster sample has the potential to set strong constraints on alternative dark energy models.

REFERENCES

Abell, G. O. 1958, ApJS, 3, 211
Abell, G. O., Corwin, H. G., Jr., & Olowin, R. P. 1989, ApJS, 70, 1
Andersson, K., et al. 2010, arXiv:1006.3068
Andreani, P., et al. 1996, ApJ, 459, L49
Alam, U., Lukić, Z., & Bhattacharya, S. 2010, arXiv:1004.0437
Alimi J., Füzfa A., Boucher V., Rasera Y., Courtin J., Corasaniti P., 2010, mnras, 401, 775
Arnaud, M., & Evrard, A. E. 1999, MNRAS, 305, 631
Arnaud, K. A. 1996, in Astronomical Society of the Pacific Conference Series, Vol. 101, Astronomical Data Analysis Software and Systems V, ed. G. H. Jacoby & J. Barnes, 17
Arnaud, M., Pratt, G. W., Piffaretti, R., Boehringer, H., Croston, J. H., & Pointecouteau, E. 2009, arXiv:0910.1234
Asplund, M., Grevesse, N., Sauval, A. J., & Scott, P. 2009, ARA&A, 47, 481
Balucinska-Church, M. & McCammon, D. 1992, ApJ, 400, 699
Bartelmann M., Doran M., Wetterich C., 2006, aap, 454, 27
Bautz, L. P., & Morgan, W. W. 1970, ApJ, 162, L149
Benítez, N. 2000, ApJ, 536, 571
Benítez, N., et al. 2004, ApJS, 150, 1
Bertin, E., & Arnouts, S. 1996, A&AS, 117, 393
Bertin, E., SWarp Resample and Coadd Software, http://terapix.iap.fr/cplt/oldSite/soft/swarp/index.html
Birkinshaw, M. 1999, Phys. Rep., 310, 97
Birkinshaw, M., Gull, S. F., & Hardebeck, H. 1984, Nature, 309, 34
Blakeslee, J. P., et al. 2003, ApJ, 596, L143
Blanton, M. R., et al. 2003, ApJ, 592, 819
Böhringer, H., et al. 2004, A&A, 425, 367
Bonamente, M., Joy, M. K., Carlstrom, J. E., Reese, E. D., & LaRoque, S. J. 2004, ApJ, 614, 56
Brodwin, M., et al. 2010, arXiv:1006.5639
Bruzual, G., & Charlot, S. 2003, MNRAS, 344, 1000
Carlstrom, J. E., Joy, M., & Grego, L. 1996, ApJ, 456, L75
Carlstrom, J. E., Holder, G. P., & Reese, E. D. 2002, ARA&A, 40, 643
Carlstrom, J. E., et al. 2009, arXiv:0907.4445
Cayón, L., Gordon, C., & Silk, J. 2010, arXiv:1006.1950
Coleman, G. D., Wu, C.-C., & Weedman, D. W. 1980, ApJS, 43, 393
Dawson, K. S., Holzapfel, W. L., Carlstrom, J. E., Joy, M., & LaRoque, S. J. 2006, ApJ, 647, 13
de Grandi, S., et al. 1999, ApJ, 514, 148
de Vaucouleurs, G. 1948, Annales d'Astrophysique, 11, 247
Duffy, A. R., Schaye, J., Kay, S. T., & Dalla Vecchia, C. 2008, MNRAS, 390, L64
Edge, A. C., et al. 1994, A&A, 289, L34
Fowler, J. W., et al. 2007, Appl. Opt., 46, 3444
Fowler, J. W., et al. 2010, arXiv:1001.2934
Fukazawa, Y., Makishima, K., & Ohashi, T. 2004, PASJ, 56, 965
Gomez, P., et al. 2004, Plasmas in the Laboratory and in the Universe: New Insights and New Challenges, 703, 361
Guzzo, L., et al. 1999, The Messenger, 95, 27
Haehnelt, M. G., & Tegmark, M. 1996, MNRAS, 279, 545
Halverson, N. W., et al. 2009, ApJ, 701, 42
Hilton, M., et al. 2009, ApJ, 697, 436
Hincks, A. D., et al. 2009, arXiv:0907.0461

High, F. W., et al. 2010, arXiv:1003.0005
Infante, L. et al. 2010, in prep
Jones, D. H., et al. 2009, MNRAS, 399, 683
Kalberla, P. M. W., Burton, W. B., Hartmann, Dap, Arnal, E. M., Bajaja, E., Morras, R., & Pöppel, W. G. L. 2005, A&A, 440, 775
Komatsu, E., & Spergel, D. N. 2001, Phys. Rev. D, 63, 063002
Komatsu, E., et al. 2009, ApJS, 180, 330
Komatsu, E., et al. 2010, arXiv:1001.4538
Kosowsky, A. 2006, New Astronomy Reviews, 50, 969
Kinney, A. L., Calzetti, D., Bohlin, R. C., McQuade, K., Storchi-Bergmann, T., & Schmitt, H. R. 1996, ApJ, 467, 38
Lo Verde, M., Miller, A., Shandera, S., & Verde, L. 2008, Journal of Cosmology and Astro-Particle Physics, 4, 14
Lueker, M., et al. 2009, arXiv:0912.4317
Martini, P., Mulchaey, J. S., & Kelson, D. D. 2007, ApJ, 664, 761
McInnes, R. N., Menanteau, F., Heavens, A. F., Hughes, J. P., Jimenez, R., Massey, R., Simon, P., & Taylor, A. 2009, MNRAS, 399, L84
Melin, J.-B., Bartlett, J. G., & Delabrouille, J. 2006, A&A, 459, 341
Menanteau, F., et al. 2010, arXiv:1002.2226
Menanteau, F., et al. 2009, ApJ, 698, 1221
Menanteau, F., & Hughes, J. P. 2009, ApJ, 694, L136
Marriage, T. A., et al. 2010, in prep
Mewe, R., Gronenschild, E. H. B. M., & van den Oord, G. H. J. 1985, A&AS, 62, 197
Motl, P. M., Hallman, E. J., Burns, J. O., & Norman, M. L. 2005, ApJ, 623, L63
Murphy, T., et al. 2010, MNRAS, 402, 2403
Mullis, C. R., Rosati, P., Lamer, G., Böhringer, H., Schwope, A., Schuecker, P., & Fassbender, R. 2005, ApJ, 623, L85
Nagai, D. 2006, ApJ, 650, 538
Niemack, M. D., et al. 2008, Journal of Low Temperature Physics, 151, 690
Plagge, T., et al. 2010, ApJ, 716, 1118
Reid, B. A., & Spergel, D. N. 2006, ApJ, 651, 643
Rosati, P., et al. 2009, A&A, 508, 583
Rosati, P., et al. 2004, AJ, 127, 230
Rose, J. A., Gaba, A. E., Christiansen, W. A., Davis, D. S., Caldwell, N., Hunstead, R. W., & Johnston-Hollitt, M. 2002, AJ, 123, 1216
Schechter, P. 1976, ApJ, 203, 297
Schlegel, D. J., Finkbeiner, D. P., & Davis, M. 1998, ApJ, 500, 525
Sehgal, N., et al. 2010, in prep
Sérsic, J. L. 1974, Ap&SS, 28, 365
Sharp, M. K., et al. 2010, ApJ, 713, 82
Skrutskie, M. F., et al. 2006, AJ, 131, 1163
Smith, J. A., Allam, S. S., Tucker, D. L., Stute, J. L., Rodgers, C. T., & Stoughton, C. 2007, AJ, submitted.
Staniszewski, Z., et al. 2009, ApJ, 701, 32
Stanford, S. A., et al. 2006, ApJ, 646, L13
Sunyaev, R. A., & Zeldovich, Y. B. 1972, Comments on Astrophysics and Space Physics, 4, 173
Swetz et al. 2010, being submitted.
Tinker, J., Kravtsov, A. V., Klypin, A., Abazajian, K., Warren, M., Yepes, G., Gottlöber, S., & Holz, D. E. 2008, ApJ, 688, 709
Tucker, W., et al. 1998, ApJ, 496, L5
Vanderlinde, K., et al. 2010, arXiv:1003.0003
Voges, W., et al. 1999, A&A, 349, 389
Vikhlinin, A., Markevitch, M., Murray, S. S., Jones, C., Forman, W., & Van Speybroeck, L. 2005, ApJ, 628, 655
Vikhlinin, A., et al. 2009, ApJ, 692, 1033
Weiland, J. L., et al. 2010, arXiv:1001.4731
Werner, N., Churazov, E., Finoguenov, A., Markevitch, M., Burenin, R., Kaastra, J. S., Böhringer, H. 2007, A&A, 474, 707
Yan, M., Sadeghpour, H. R., & Dalgarno, A. 1998, ApJ, 496, 1044
Zhang, Y.-Y., Böhringer, H., Finoguenov, A., Ikebe, Y., Matsushita, K., Schuecker, P., Guzzo, L., & Collins, C. A. 2006, A&A, 456, 55